

1 **Multi-Machine Learning Ensemble Regionalization of Hydrological**  
2 **Parameters for Enhancing Flood Prediction in Ungauged**  
3 **Mountainous Catchments**

4  
5 Kai Li, Linmao Guo, Genxu Wang\*, Jihui Gao\*, Xiangyang Sun, Peng Huang,  
6 Jinlong Li, Jiapei Ma, Xinyu Zhang

7  
8 *State Key Laboratory of Hydraulics and Mountain River Engineering, College of Water Resource  
9 and Hydropower, Sichuan University, Chengdu, 610000, China*

10 \*Corresponding author: Genxu Wang (wanggx@scu.edu.cn) and Jihui Gao (jgao@scu.edu.cn).

11

12 **Abstract:**

13 Machine learning-based parameter regionalization is an important method for  
14 flood prediction in ungauged mountainous catchments. However, single machine  
15 learning parameter regionalization often exhibits limitations in prediction accuracy and  
16 robustness. Therefore, this study proposes a multi-machine learning ensemble  
17 regionalization method that integrates Gradient Boosting Machine (GBM), K-Nearest  
18 Neighbors (KNN), and Extremely Randomized Trees (ERT) methods (GBM-KNN-  
19 ERT) to regionalize the sensitive parameters of the Topography-Based Subsurface  
20 Storm Flow (Top-SSF) model. Validated across 80 mountainous catchments in  
21 southwestern China, the GBM-KNN-ERT method demonstrates superior performance  
22 with 90% of ungauged catchments achieving the Nash-Sutcliffe Efficiency (NSE)  
23 above 0.9, representing a 67.44% improvement over the best single machine learning  
24 parameter regionalization. Notably, the GBM-KNN-ERT method shows improved  
25 robustness to climate change and changes in the number of donor catchments compared  
26 to other regionalization methods. An optimal balance between accuracy and

27 computational efficiency was achieved using 20-40 high quality donor catchments  
28 (NSE greater than 0.85). This study provides systematic evidence that multi-machine  
29 learning ensemble can effectively address regionalization challenges in ungauged  
30 mountainous regions, offering a reliable tool for water resource management and flood  
31 disaster mitigation.

32 **Keywords:** Flood forecasting; Regionalization; Ungauged mountainous catchments;  
33 Top-SSF model;

34

35 **Highlights:**

36 1. Proposes a novel multi-machine learning ensemble regionalization method  
37 2. The GBM-KNN-ERT method increases the percentage of catchments with high-  
38 accuracy flood predictions (NSE >0.9) to 90%, which is a 67.44% improvement  
39 over the best single machine learning method.  
40 3. The GBM-KNN-ERT method exhibits greater stability under climate change.

41

42 **1. Introduction**

43 Floods in mountainous catchments, encompassing both flash floods and general  
44 larger-scale flood events which can be derived from mountainous upland catchments,  
45 pose a significant threat to human safety and property, particularly in regions lacking  
46 sufficient observational data (Luo et al., 2015; Zhai et al., 2018). While hydrological  
47 models like the Topography-Based Subsurface Storm Flow (Top-SSF) model (Li et al.,  
48 2024) offer promising simulation capabilities, their application in ungauged catchments  
49 is severely limited by the absence of calibration data (Choi et al., 2023; Liu et al., 2018).  
50 Effective parameter regionalization methods are therefore essential for transferring  
51 hydrological knowledge from gauged to ungauged regions, enabling reliable flood  
52 prediction in ungauged mountainous catchment (Garambois et al., 2015; Ragettli et al.,  
53 2017; Xu et al., 2018).

54 Parameter regionalization is a crucial method for flood prediction in ungauged  
55 catchments (Arsenault et al., 2022; Guo et al., 2021; Kratzert et al., 2019; Zhang et al.,  
56 2020). Compared to purely data-driven methods, parameter regionalization offers  
57 enhanced physical interpretability (Nearing et al., 2024; Tang et al., 2023; Zhang et al.,  
58 2024). Existing parameter regionalization methods can be broadly classified into three  
59 categories: similarity-based, hydrological signatures-based, and regression-based  
60 (Arsenault et al., 2019; Wu et al., 2022). Similarity-based methods rely on the  
61 assumption that catchments with similar characteristics exhibit similar hydrological  
62 responses, considering spatial proximity (Arsenault et al., 2019; Pugliese et al., 2018;  
63 Yang et al., 2018) and physical similarity (similar climatic and land cover conditions

64 have similar hydrological characteristics) (Kanishka et al., 2017; Papageorgaki et al.,  
65 2016). Hydrological signature-based methods use hydrological signatures (quantitative  
66 metrics that describe statistical or dynamic properties of streamflow) as an intermediate  
67 link, establishing relationships first between model parameters and signatures, and then  
68 between signatures and catchment descriptors to facilitate parameter transfer  
69 (McMillan, 2021; Zhang et al., 2018). Regression-based methods, which directly link  
70 hydrological model parameters to catchment descriptors, are widely used due to their  
71 simplicity and computational efficiency (Guo et al., 2021; Kratzert et al., 2019; Song et  
72 al., 2022; Wu et al., 2022). However, the performance of regression-based methods is  
73 frequently constrained by the inherent nonlinearity in the relationships between model  
74 parameters and catchment descriptors, coupled with the difficulty in adequately  
75 capturing spatial heterogeneity, especially within complex mountainous terrain (Wu et  
76 al., 2022).

77 Recent advances in machine learning offer potential solutions by capturing  
78 nonlinear patterns in high-dimensional data. Methods such as Decision Tree (DT),  
79 Extremely Randomized Trees (ERT), Gradient Boosting Machine (GBM), K-Nearest  
80 Neighbor (KNN), Random Forest (RF), and Support Vector Machines (SVM) have  
81 shown promise in parameter regionalization (Golian et al., 2021; Song et al., 2022).  
82 However, existing machine learning-based parameter regionalization studies  
83 predominantly focus on runoff prediction at coarser temporal scales (daily or monthly)  
84 (Li et al., 2022; Wu et al., 2022), leaving a significant gap in high-resolution (hourly or  
85 sub-hourly) flood prediction in ungauged mountainous catchments. Moreover, these

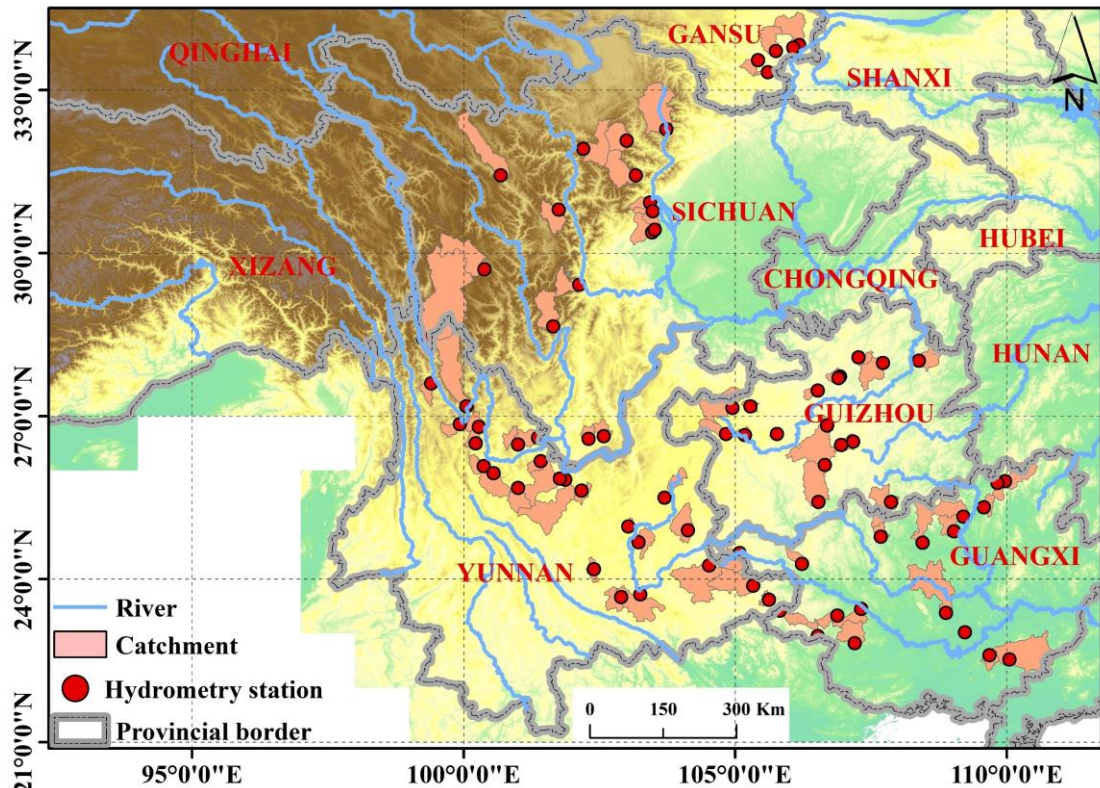
86 studies often rely on single machine learning methods to estimate all hydrological  
87 model parameters (Golian et al., 2021; Song et al., 2022; Wu et al., 2022). Given that  
88 different machine learning methods operate on distinct principles (Jordan et al., 2015;  
89 Zounemat-Kermani et al., 2021) and hydrological model parameters represent diverse  
90 hydrological processes (Li et al., 2024), a single machine learning method may not  
91 adequately capture the complexity of model parameter estimation (Golian et al., 2021;  
92 Wu et al., 2022). Therefore, exploring the multi-machine learning ensemble methods is  
93 essential to improve the accuracy of high-resolution flood prediction in ungauged  
94 mountainous catchments.

95 Southwest China's mountainous regions are particularly vulnerable to frequent  
96 floods, leading to ecosystem degradation through habitat disruption and biodiversity  
97 loss (Gan et al., 2018). The abundance of ungauged catchments in this region poses a  
98 significant challenge to reliable flood prediction. To address this critical issue, we  
99 systematically evaluate the performance of a novel multi-machine learning ensemble  
100 method for regionalizing Top-SSF model parameters across 80 representative  
101 catchments (mean area: 1,586 km<sup>2</sup>) in Southwest China. By assessing ensemble method  
102 robustness under climate change and with varying donor catchment configurations, this  
103 study aims to significantly enhance flood prediction accuracy in ungauged mountainous  
104 catchments, contributing to improved ecosystem resilience, enhanced human safety,  
105 and more effective water resource management in the face of escalating climatic  
106 pressures.

107 **2. Study area and datasets**

108 **2.1. Study area**

109 This study investigated 80 mountainous catchments in Southwestern China,  
110 encompassing Sichuan, Yunnan, Guangxi, Guizhou, and Chongqing provinces (Fig. 1).  
111 This region exhibits diverse climatic zones, including subtropical monsoon, plateau  
112 mountain, and tropical monsoon climates. The selected catchments have an average  
113 area of 1,586 km<sup>2</sup> (ranging from 109 to 6,564 km<sup>2</sup>), with elevations ranging from 63 to  
114 6,284 meters. Mean annual temperature varies from 15 to 20°C, and annual  
115 precipitation ranges from 1,200 to 1,800 mm (Li et al., 2016), with approximately 80%  
116 of the annual precipitation occurring during summer and autumn, contributing to  
117 frequent flooding events (Cheng et al., 2019). These catchments are situated within a  
118 heavily forested region, the second largest in China (Hua et al., 2018), with forest cover  
119 ranging from 3% to 92% (mean: 51%), influencing evapotranspiration and runoff  
120 generation. Dominant soil types, according to the Genetic Soil Classification of China  
121 (Shi et al., 2004), include purple soil (12.20%), yellow soil (11.39%), and red soil  
122 (9.52%), each with distinct hydrological properties.



123

124 **Fig.1.** Geographical distribution of the 80 gauged catchments used, with locations of  
 125 hydrometry station (red points) and major rivers indicated.

126 **2.2. Datasets**

127 Hourly flow data (2015–2018) for 80 mountainous catchments in China were  
 128 sourced from the Hydrological Bureau of the Ministry of Water Resources, through  
 129 China's hydrologic yearbooks, encompassing a spectrum of events from flash floods  
 130 and general floods which can be derived from mountainous upland catchments. Hourly  
 131 rainfall data (2015–2018) were obtained from ground meteorological stations across  
 132 China (<http://en.weather.com.cn>), providing crucial input for hydrological modelling.  
 133 Additional meteorological variables, including temperature, wind speed, dewpoint  
 134 temperature, and surface net solar radiation, were obtained from the ERA5 hourly  
 135 dataset (1940–present) (Hersbach et al., 2023), ensuring comprehensive atmospheric  
 136 forcing. Relative humidity was estimated using dewpoint temperature. Historical

137 (1901–2021) and projected future (SSP585, 2022–2100) temperature and precipitation  
138 data for China, averaged from the EC-Earth3, GFDL-ESM4, and MRI-ESM2-0 models  
139 at 1 km resolution, were obtained from "A Big Earth Data Platform for Three Poles" to  
140 assess the impact of climate change (Ding et al., 2020) (<http://poles.tpdc.ac.cn>).  
141 Topographic data, including a 30m resolution Digital Elevation Model (DEM), used for  
142 river network and topographic index derivation, were obtained from EARTHDATA  
143 (<https://search.earthdata.nasa.gov/search>). Forest cover data (30m resolution) were  
144 sourced from the Global Forest Cover and Forest Change Map  
145 (<https://www.noda.ac.cn/>), providing information on vegetation characteristics. Bulk  
146 density (BD) data were derived from the Soil Database of China for Land Surface  
147 Modelling (Dai et al., 2013). Soil hydraulic parameters, specifically saturated hydraulic  
148 conductivity (Ks\_CH) for Clapp and Hornberger functions and the pore-connectivity  
149 parameter (L) for van Genuchten and Mualem functions, were acquired from the China  
150 Dataset of Soil Hydraulic Parameters Using Pedotransfer Functions for Land Surface  
151 Modeling (Shangguan et al., 2013).  
152

153 **Table 1.** Model forcing data and catchment descriptors information.

Data type	Name	Unit	Function
Hydro-meteorology	Rainfall	mm	Input for hydrological model
	Flood	m <sup>3</sup> /s	Used for model calibration (hourly resolution)
	Temperature	K	
	Surface pressure	Pa	
	Dewpoint temperature	K	
	wind speed	m/s	
	Surface net solar radiation	J/m <sup>2</sup>	Input for hydrological model
	Relative humidity	%	
	1 km monthly precipitation (1901-2021)	mm	
	1 km monthly temperature (1901-2021)	°C	
Soil characteristics	1 km monthly temperature (2022-2100, SSP5-8.5, EC-Earth3, GFDL-ESM4, MRI-ESM2-0)	°C	Multi-year surface average as catchment descriptors
	1 km monthly precipitation (2022-2100, SSP5-8.5, EC-Earth3, GFDL-ESM4, MRI-ESM2-0)	mm	
	Soil bulk density (BD)	g/cm <sup>3</sup>	
	Pore-connectivity parameter (L) for the van Genuchten and Mualem functions	-	
Topography	Saturated hydraulic conductivity (Ks_CH) of the Clapp and Hornberger Functions	cm d <sup>-1</sup>	Surface average as catchment descriptors
	Forest cover (FC)	%	
	DEM	m	
	Topographic index	-	
	Slope	mm <sup>-1</sup>	
	Catchment area	km <sup>2</sup>	

154 

### 3. Methodology

155 

#### 3.1. Hydrological model

156 Top-SSF is a semi-distributed hydrological model based on the well-established

157 TOPMODEL framework, which delineates sub-basins based on the topographic index.

158 It retains the key advantages of TOPMODEL, such as its parsimonious structure,

159 physical interpretability, and ease of parameter transfer (Beven et al., 2021; Gao et al.,

160 2018), consists of 15 parameters representing six key hydrological components: canopy

161 interception, infiltration, evapotranspiration, unsaturated zone moisture transport,

162 subsurface storm flow, and flow routing (Li et al., 2024). In the Top-SSF model, flood

163 can be comprised of four components: infiltration-excess overland flow, saturation-

164 excess overland flow, subsurface storm flow, and groundwater discharge.

165 Infiltration-excess overland flow occurs when the rainfall intensity exceeds the

166 infiltration capacity. In this study, infiltration is simulated using the Green-Ampt model.  
 167 When surface ponding occurs, the infiltration rate is determined by solving the Green-  
 168 Ampt equation iteratively, for which the Newton-Raphson method is employed. The  
 169 infiltration rate ( $f_{in}$ ) is given by:

$$170 \quad f_{in} = -\frac{Ks(CD+F_{satrt})}{Szm(1-e^{(F_{satrt}/Szm)})} \quad (1)$$

171 where,  $f_{in}$  is the infiltration rate (m/h);  $Ks$  is surface hydraulic conductivity (m/h);  
 172  $CD$  is capillary drive (m);  $F_{satrt}$  is the initial cumulative infiltration (m);  $Szm$  is the  
 173 maximum water storage capacity in the unsaturated zone (m).

174 Saturation excess overland flow occurs at computational cell  $i$  when the  
 175 groundwater table depth,  $S_i$  is less than or equal to zero (i.e.,  $S_i \leq 0$ , indicating the  
 176 water table has reached the surface). It is calculated as:

$$177 \quad r_{s,i} = \max\{Suz_i - \max(S_i, 0), 0\} \quad (2)$$

178 where,  $r_{s,i}$  is the depth of saturation excess overland flow generated at cell  $i$  (m);  $Suz_i$   
 179 is the soil water storage in the unsaturated zone, at cell  $i$  (m);  $S_i$  is the groundwater table  
 180 depth at cell  $i$  (m).

181 The depth of subsurface storm flow generated at computational cell  $i$ ,  $r_{sf,i}$  is  
 182 given by:

$$183 \quad r_{sf,i} = q_{sf0}(1 - S_{sf,i}/S_{fmax}) \quad (3)$$

184 where,  $r_{sf,i}$  is the depth of subsurface storm flow at cell  $i$  (m);  $q_{sf0}$  is initial subsurface  
 185 storm flow (m);  $S_{sf,i}$  is the water storage deficit in the subsurface storm flow zone at  
 186 cell  $i$  (m).

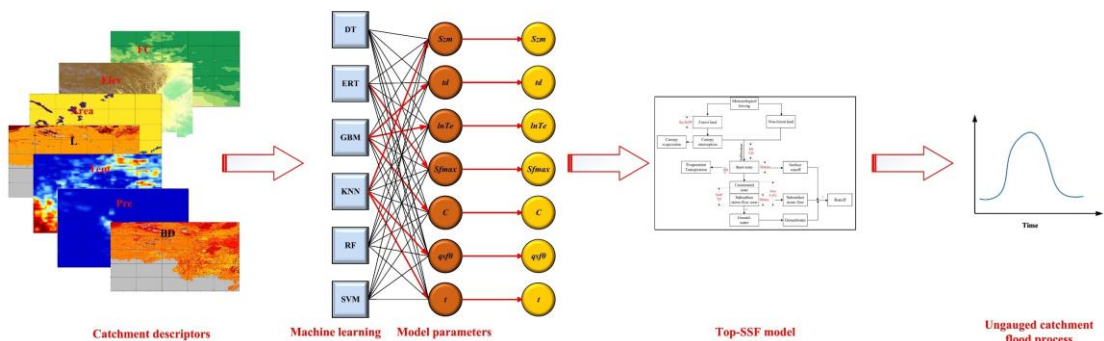
187 The depth of groundwater discharge is calculated as:

$$188 \quad r_b = e^{\ln Te - \lambda - \bar{S}_g/Szm} \quad (4)$$

189 where,  $r_b$  is depth of groundwater discharge (m);  $\ln Te$  is the log of the areal average of  
 190  $T0$  ( $m^2/h$ );  $\lambda$  is the catchment average topographic index;  $\bar{S}_g$  is the catchment average  
 191 groundwater table depth (m). For the complete set of equations for the Top-SSF model,  
 192 the reader is referred to the Supplementary Material and (Li et al., 2024).

193 **3.2. Multi-machine learning ensemble method**

194 To improve flood prediction accuracy in ungauged mountainous catchments, we  
 195 proposed a multi-machine learning ensemble method for regionalizing sensitive  
 196 parameters of the Top-SSF model. This method leverages the complementary strengths  
 197 of multi-machine learning methods to estimate model parameters based on catchment  
 198 descriptors (Fig. 2). The characteristics, strengths, and limitations of each machine  
 199 learning method are summarized in Table 2. The ensemble method employs a cross-  
 200 validation procedure to select the best-performing machine learning method for each  
 201 sensitive parameter. These selections are then integrated into a unified regionalization  
 202 scheme. By mitigating limitations inherent in single machine learning regionalization,  
 203 such as model bias and overfitting, and by capturing complex hydrological processes  
 204 in mountainous catchment, this ensemble method aims to achieve more accurate flood  
 205 prediction in ungauged catchments.



207 **Fig.2.** Multi-machine learning ensemble method for regionalization in ungauged mountainous  
 208 catchments. The red line indicates the machine learning method that yielded the optimal  
 209 parameter estimates.

210

211 **Table 2.** Seven machine learning model characteristics, advantages and disadvantages.

Machine learning	Characteristic	Advantage	Disadvantages
DT	A single decision tree hierarchically partitions the data space using a tree structure, with internal nodes representing features, branches representing decision rules, and leaf nodes representing class labels.	High interpretability; Minimal data preprocessing.	Unstable; Tends to overfit.
ERT	Construct multiple decision trees with randomly selected feature values and randomly divided nodes (Geurts et al., 2006).	Low overfitting risk; Computational efficiency; Resilient to noise.	Possibility of increased bias; Limited interpretability.
GBM	Construct multiple decision trees. Multiple weak learners are trained iteratively and the loss function is optimised using gradient descent, progressively combined into a robust model through the learning rate (Friedman, 2002).	High accuracy for structured data; Robust to outliers; Minimal data preprocessing.	Limited interpretability; Complex adjustments.
KNN	It is a non-parametric, instance-based supervised learning algorithm. It operates by finding the K nearest data points in the training data to a given data point and making predictions based on these (Wani et al., 2017).	Simple and easy to implement. Learning process is quick.	Sensitivity to noisy and scale of data. Accuracy can be heavily impacted by the choice of K.
RF	A bagging algorithm proposed by Breiman (2001) that uses ensemble learning. Involves training numerous decision trees and aggregating predictions.	Simple and easy to implement; Low computational cost.	Prone to overfitting in noisy regression tasks.
SVM	Identifies hyperplanes in high-dimensional spaces to segregate data. The optimal hyperplane maximizes the margin between it and the nearest data points, termed support vectors (Sain, 1996).	Uses kernel functions to address nonlinear classification issues.	Sensitive to noise

212 **3.3. Parameter regionalization process**

213 The parameter regionalization process comprised four key steps: (1) Top-SSF  
 214 model calibration and parameter sensitivity analysis; (2) selection of relevant catchment  
 215 descriptors; (3) establishment of regionalization relationships between sensitive model  
 216 parameters and catchment descriptors using multi-machine learning ensemble methods;  
 217 and (4) evaluation of parameter regionalization performance.

218 **3.3.1. Top-SSF model calibration and parameter sensitivity analysis**

219 In this study, the Top-SSF model was employed to simulate hydrological processes.  
 220 The model was driven by continuous hourly meteorological data, including rainfall,  
 221 temperature, surface pressure, relative humidity, wind speed, and surface net solar  
 222 radiation. For each catchment, model parameters were calibrated using two  
 223 hydrologically independent and representative flood events. A third, distinct flood

224 event was then used for model validation. The Nash-Sutcliffe Efficiency (NSE) served  
225 as the objective function during calibration, with parameter optimization achieved  
226 using the Shuffled Complex Evolution (SCE-UA) algorithm (Duan et al., 1994), known  
227 for its global convergence and robustness (Dakhlaoui et al., 2012; Qi et al., 2016).  
228 Model performance was evaluated using the NSE, the relative error of flood peak flow  
229 (Qp), and the absolute error in flood peak occurrence time (Tp), following China's  
230 Specification for Hydrological Information Forecast (GB/T 22482-2008). These  
231 metrics quantify the model's ability to predict flood dynamics, peak flow, and timing.  
232 Following calibration, a sensitivity analysis was conducted to identify and exclude  
233 insensitive model parameters (Lenhart et al., 2002), which were then used for  
234 regionalization. This approach reduces the dimensionality of the regionalization  
235 problem and improves the efficiency of the process.

236 The sensitivity index ( $Si$ ) of each hydrological model parameter was determined  
237 using the method of Lenhart et al. (2002), which assesses the influence of  $\pm 10\%$   
238 changes in parameter values (Eq. 5). Table 3 outlines the sensitivity analysis results for  
239 the model parameters across the 80 mountainous catchments. The  $Si$  values are  
240 categorized as follows (Guo et al., 2022): negligible sensitivity ( $|Si| < 0.05$ ),  
241 moderate sensitivity ( $0.05 < |Si| < 0.2$ ), high sensitivity ( $0.2 < |Si| < 1.00$ ), and  
242 extremely high sensitivity ( $|Si| \geq 1.00$ ). Based on the sensitivity analyses, seven  
243 sensitive model parameters were identified:  $Szm$ ,  $lnTe$ ,  $Sfmax$ ,  $C$ ,  $qsf0$ ,  $t$  (Table 3).

$$244 Si = \frac{1}{N} \sum_t^N \frac{(y_2(t) - y_1(t))/y_0(t)}{2\Delta x/x_0} \quad (5)$$

245 where  $y_0(t)$  is the flood value of the calibrated parameter  $x_0$  at time  $t$ ;  $\Delta x$  is the

246 adjusted parameter difference,  $\Delta x/x_0=10\%$ ;  $y_1(t)$  is the flood value of the calibrated  
 247 parameter  $x_0 - \Delta x$  at time  $t$ ;  $y_2(t)$  is the flood value of the calibrated parameter  $x_0 +$   
 248  $\Delta x$  at time  $t$ .

249 **Table 3.** Top-SSF model main modules and default range of parameters.

Module	Parameter	Definition	Unit	Default range	Sensitivity index
Canopy interception	$Sc$	Canopy storage capacity	m	0.00~0.01	<0.05
	$St$	Trunk storage capacity	m	0.00~0.01	<0.05
	$Pt$	Proportion of rain diverted into stemflow per cover	%	0.00~1.00	<0.05
Evapotranspiration	$Sr0$	Initial root zone storage deficit	m	0.00~0.02	<0.05
	$Srmax$	Maximum root zone storage deficit	m	0.00~2	<0.05
Infiltration	$Ks$	Surface hydraulic conductivity	m/h	0~0.01	<0.05
	$CD$	Capillary drive (Morel-Seytoux et al., 1974)	m	0~5	<0.05
Unsaturated zone	$Suz0$	Initial baseflow per unit area	m	0.00~ $10^{-4}$	<0.05
	$Szm$	Soil maximum water storage capacity	m	0.00~1.00	<b>0.19</b>
	$td$	Unsaturated zone time delay per unit storage deficit	h/m	0~3	<b>1.07</b>
	$lnTe$	log of the areal average of T0	$m^2/h$	-2.00~1.00	<b>3.4</b>
Subsurface storm flow zone	$Sfmax$	Maximum subsurface storm flow zone deficit	m	0.00~0.01	<b>0.16</b>
	$C$	Transfer coefficient	$m^2/h$	0.00~0.1	<b>0.26</b>
	$qsf0$	Initial subsurface storm flow per unit area	m	0.00~0.02	<b>0.18</b>
Routing	$t$	Flow routing correction coefficient	-	0.00~5.0	<b>1.21</b>

250 **Note, the bolded values in the sensitivity index indicate sensitive model parameters (i.e.,**  
 251  **$|Si|>0.05$ .**

252 **3.3.2. Catchment descriptor selection**

253 To mitigate the effects of multicollinearity on the accuracy and reliability of the  
 254 parameter regionalization methods, catchment descriptors were screened using the  
 255 variance inflation factor (VIF) and correlation coefficients. A VIF threshold of less than  
 256 10 (VIF < 10) was used to indicate acceptably low multicollinearity (Salmeron et al.,  
 257 2018). Initial screening identified strong correlations between several descriptor pairs,

258 notably L with Ks\_CH, and Tem with Elev. Furthermore, the VIF values for Ks\_CH  
 259 and Slope were found to exceed 10. Consequently, Ks\_CH and Slope were removed  
 260 from the potential set of descriptors. Following their removal, a re-evaluation of the  
 261 VIF for the remaining descriptors was conducted. Although a notable correlation exists  
 262 between Tem and elevation (Elev), their VIF values in the reduced set were both below  
 263 the threshold of 10. Given the importance of Tem for representing climate impacts and  
 264 Elev as a key topographic driver, both were retained to preserve potentially valuable  
 265 information. The final set of seven catchment descriptors selected for regionalization  
 266 therefore comprised FC, Elev, Area, L, Tem, Pre, and BD. As illustrated in Fig. 3b, the  
 267 correlations among these final descriptors and the sensitive model parameters are  
 268 generally low (highest at 0.5), suggesting that the relationships are complex and  
 269 nonlinear.

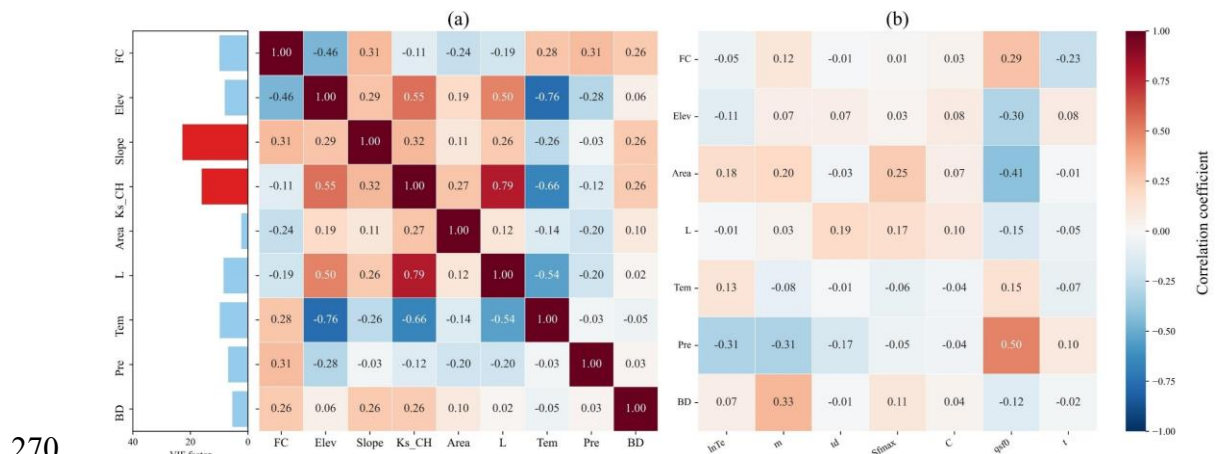


**Fig.3.** Analysis of catchment descriptor relationships: (a) Correlation coefficients and variance inflation factors (VIF) among all descriptors; (b) Correlation coefficients between sensitive model parameters and descriptors with VIF values below 10.

### 3.3.3. Parameter regionalization

275 To simulate ungauged catchment conditions, each of the 80 catchments was  
 276 iteratively treated as an ungauged catchment, with the remaining 79 catchments serving

277 as donor catchments. A parameter regionalization method was then constructed using  
278 the catchment descriptors and sensitive model parameters of the donor catchments to  
279 predict the seven sensitive model parameters for the ungauged catchment based on its  
280 catchment descriptors. These predicted model parameters were then input into the Top-  
281 SSF model to enable flood prediction in ungauged catchments. To ensure robust and  
282 generalizable results, K-fold cross-validation (K = 10) was implemented. This involved  
283 randomly partitioning the 79 donor catchments into K subsets, using one subset as a  
284 test set and the remaining K-1 subsets for method training in each iteration (Jung, 2018).  
285 This approach maximizes data utilization and minimizes bias associated with specific  
286 data partitioning. Hyperparameter tuning for each machine learning method was  
287 performed using RandomizedSearchCV (Bergstra et al., 2012), with the objective of  
288 minimizing the difference between predicted and observed parameter values.

### 289 **3.3.4. Evaluated metrics**

290 The performance of the parameter regionalization methods was evaluated by  
291 considering two key aspects. First, the accuracy of the methods in estimating sensitive  
292 model parameters was assessed using three metrics: root mean square error (RMSE),  
293 standard deviation (STD), and the coefficient of determination ( $R^2$ ). The  $R^2$  was used  
294 to quantify the agreement between estimated and calibrated parameter sets. Second, to  
295 evaluate the impact of parameter regionalization on flood prediction. The resulting  
296 flood predictions were then evaluated using the NSE, Qp, and Tp metrics.

$$297 NSE = 1 - \frac{\sum_{j=1}^M (Q_{obs}(j) - Q_{sim}(j))^2}{\sum_{j=1}^M (Q_{obs}(j) - \bar{Q}_{obs})^2} \quad (6)$$

$$298 Q_p = \left| \frac{Q_{obs,p} - Q_{sim,p}}{Q_{obs,p}} \times 100\% \right| \quad (7)$$

299  $T_p = |T_{obs,p} - T_{sim,p}| \quad (8)$

300 where  $Q_{obs}(j)$  is the observed flow rate ( $\text{m}^3/\text{s}$ );  $Q_{sim}(j)$  is the simulated flow rate  
301 ( $\text{m}^3/\text{s}$ );  $\bar{Q}_{obs}$  is the mean value of the observed flow rate ( $\text{m}^3/\text{s}$ );  $Q_{obs,p}$  is the observed  
302 flood peak flow ( $\text{m}^3/\text{s}$ );  $Q_{sim,p}$  is the simulated flood peak flow ( $\text{m}^3/\text{s}$ );  $T_{obs,p}$  is the  
303 observed flood peak occurrence time (h); and  $T_{sim,p}$  is the simulated flood peak  
304 occurrence time (h).

305

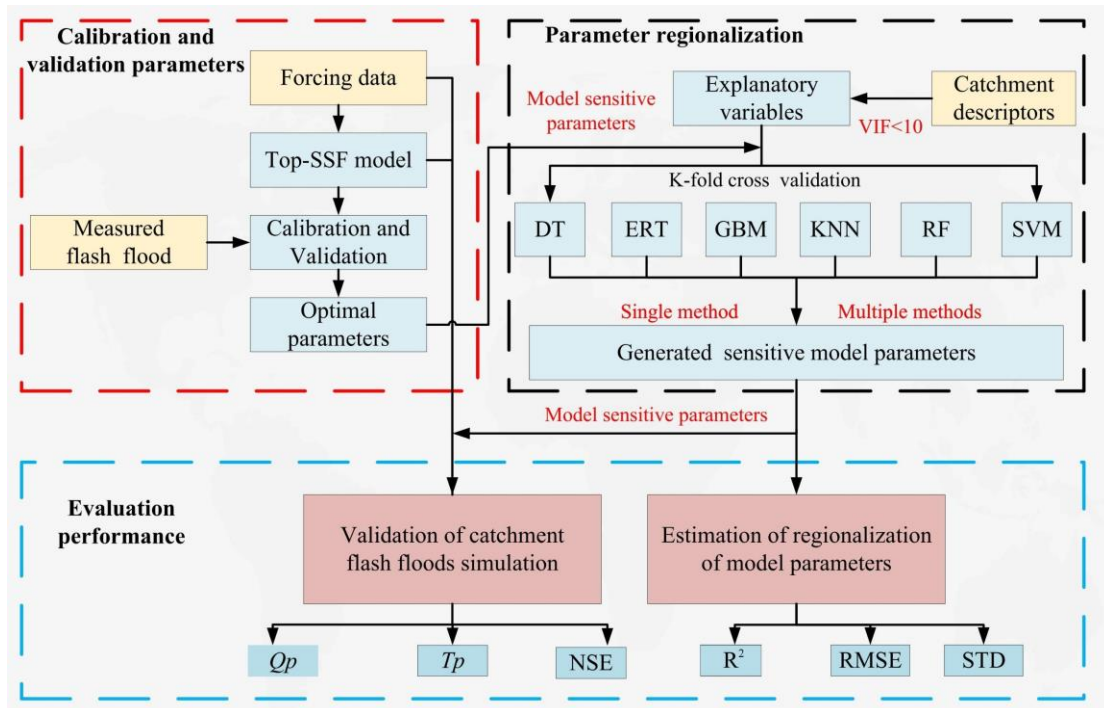
306  $RMSE = \sqrt{\frac{1}{N} \sum_{i=1}^n (X_i - Y_i)^2} \quad (9)$

307  $STD = \sqrt{\frac{1}{N-1} \sum_{i=1}^N (Y_i - \bar{Y})^2} \quad (10)$

308  $R^2 = \frac{[\sum_{i=1}^n (X_i - \bar{X})(Y_i - \bar{Y})]^2}{\sum_{i=1}^n (X_i - \bar{X})^2 \sum_{i=1}^n (Y_i - \bar{Y})^2} \quad (11)$

309 where  $X_i$  is the Top-SSF calibration model parameter value;  $Y_i$  is the model parameter  
310 estimated value using the parameter regionalization method;  $\bar{X}$  and  $\bar{Y}$  are the mean  
311 values of  $X_i$  and  $Y_i$ ;  $N$  is the sample size equal to 80.

312



313

314 **Fig.4.** Flowchart illustrating the parameter calibration, validation, and regionalization workflow.  
 315 Abbreviations: Top-SSF (Topography-Based Subsurface Storm Flow hydrological model),  
 316 DT (Decision Tree), ERT (Extremely Randomized Trees), GBM (Gradient Boosting  
 317 Machine), KNN (K-Nearest Neighbor), RF (Random Forest), SVM (Support Vector  
 318 Machine), NSE (Nash-Sutcliffe efficiency),  $R^2$  (Coefficient of Determination), Qp (The  
 319 relative error of flood peak flow), Tp (The absolute error in flood peak occurrence time),  
 320 VIF (Variance inflation factor), RMSE (Root mean square error), STD (Standard  
 321 deviation).

322

## 4. Result

323

### 4.1. Model performance

324

The Top-SSF model demonstrated good flood simulation performance across the

325

80 gauged catchments, as quantified by NSE, Qp, and Tp. During the calibration period,

326

50% of the catchments achieved NSE values exceeding 0.78 (Fig. 5a), the median Qp

327

value was below 10% (Fig. 5b), and the median Tp value was within 2 hours (Fig. 5c).

328

The average NSE value was approximately 0.8, with a maximum of 0.96. The majority

329

of Qp values were around 8%, and the majority of Tp values were below 2 hours.

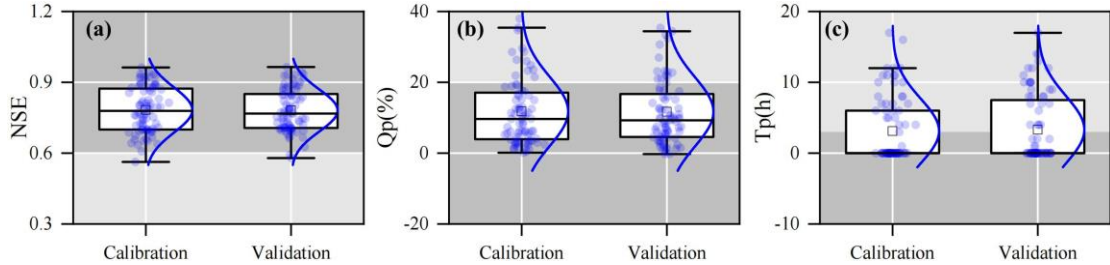
330

During the validation period, the median NSE value was 0.76 (Fig. 5a), the median Qp

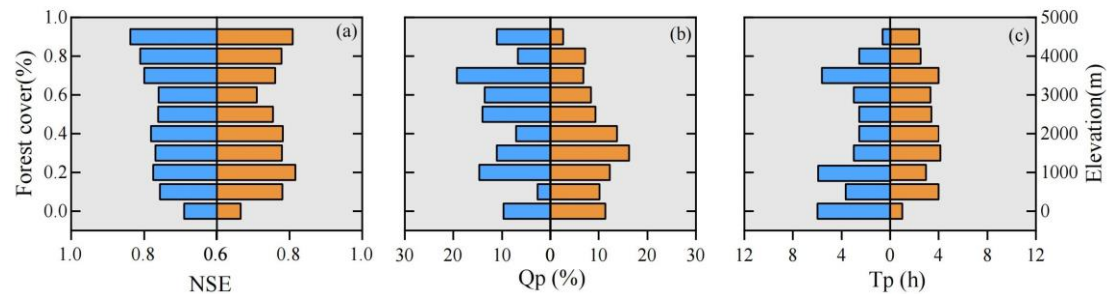
331 value was below 10% (Fig. 5b), and the median Tp value was within 4 hours (Fig.5c).  
332 The hydrological response times for the 80 catchments were approximated as the time  
333 from precipitation peak to flood peak. The estimated range is from 1 to 26 hours. This  
334 diversity is indicative of the comprehensive nature of the study, which encompasses  
335 both rapid flash floods in smaller basins and more general floods in larger, mountainous  
336 catchments (mean area: 1,586 km<sup>2</sup>). For catchments with longer response times, a  
337 median error of 2-4 hours remains operationally valuable for providing sufficient flood  
338 warning lead time. It is noteworthy that the median Tp during the calibration period  
339 (within 2 hours) satisfied China's Specification for Hydrological Information Forecast  
340 (GB/T 22482-2008) stringent requirements for high-quality forecasts.

341 Model performance also exhibited some dependence on catchment characteristics.  
342 For instance, NSE generally improved with increasing forest cover (Fig. 6a), potentially  
343 due to the model's explicit representation of forest canopy interception and subsurface  
344 storm flow generation mechanisms. The relationship between NSE, Qp, Tp and  
345 elevation was more complex, suggesting a nonlinear influence of elevation on model  
346 performance (Fig. 6 a-c). The demonstrated robust performance of the Top-SSF model  
347 provides a strong foundation for its application in subsequent parameter regionalization  
348 analyses.

349



350  
351 **Fig. 5.** Boxplots of (a) NSE, (b) Qp, and (c) Tp during the calibration and validation periods  
352 for 80 gauged catchments. The box represents the interquartile range, with the middle line  
353 indicating the median (50th percentile). The whiskers represent the minimum and  
354 maximum values. "□" represents the mean value. Dark grey indicates the range of flood  
355 prediction criteria (i.e., NSE> 0.75, Qp< 20%, and Tp < 2 hours).



356  
357 **Fig.6.** Influence of environmental factors on Top-SSF model performance in flood simulation.  
358 The graphs illustrate the relationship between model evaluation metrics and forest cover  
359 (left) and elevation (right).  
360

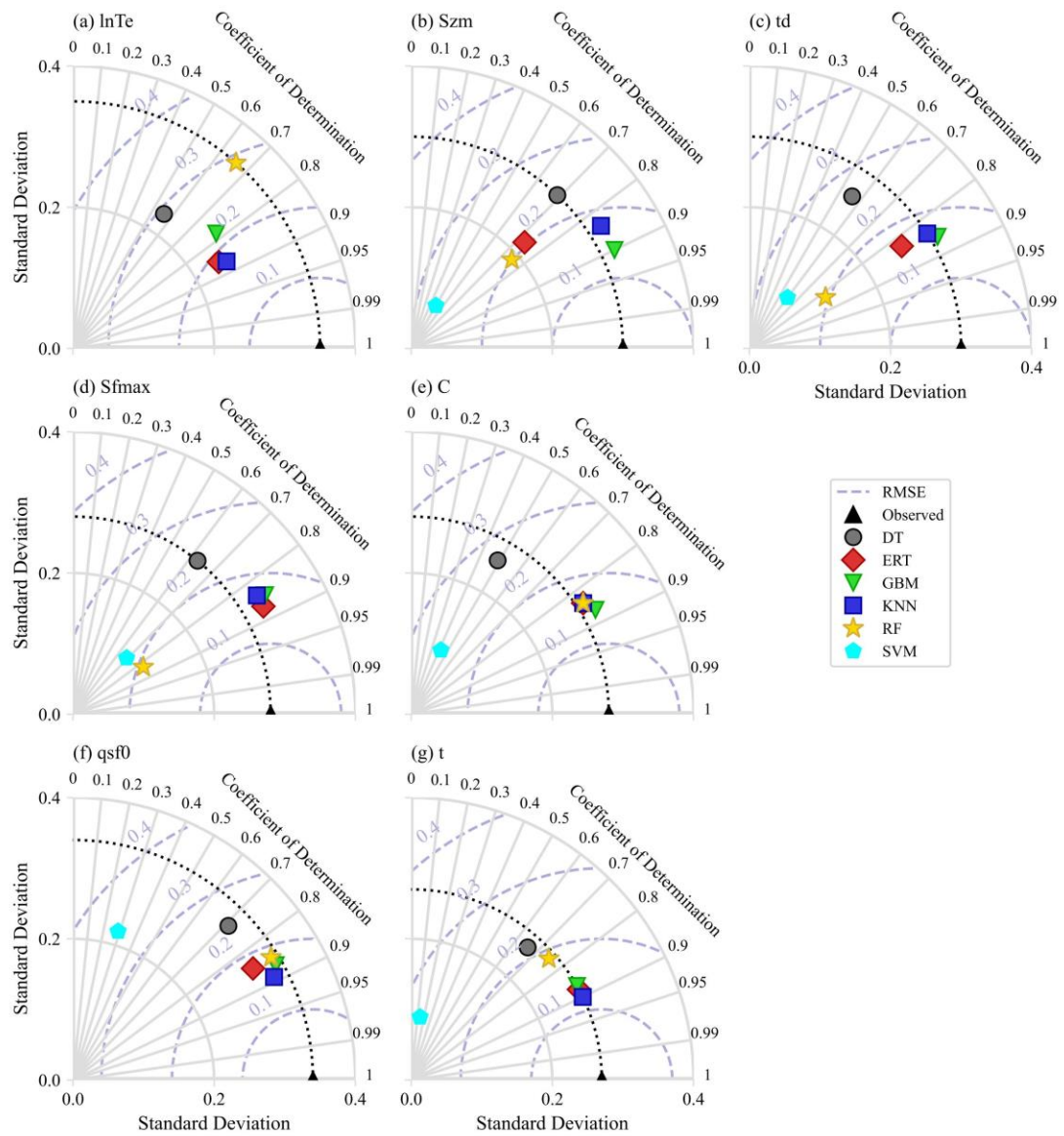
## 361 **4.2. Results of parameter regionalization**

### 362 **4.2.1. Comparison of sensitive model parameter estimates**

363 The six single machine learning regionalization methods exhibited varying  
364 performance in estimating sensitive model parameters (Fig. 7), likely due to differences  
365 in catchment descriptor characteristics and the underlying principles of each method.

366 Their hyperparameter results are presented in Tables S1–S6 of the supplementary  
367 material. The GBM demonstrated the highest accuracy in estimating  $Szm$ ,  $td$ , and  $C$   
368 ( $R^2 = 0.90$ , 0.86, and 0.87, respectively,), with its estimates also exhibiting a STD that  
369 closely matched the distribution of the calibrated parameter values. KNN provided the  
370 most accurate estimates for  $lnTe$ ,  $qsf0$ , and  $t$  ( $R^2 = 0.87$ , 0.89, and 0.90, respectively),  
371 also with STD closely resembling the calibrated parameter distributions. ERT

372 performed best in estimating  $Sfmax$  ( $R^2 = 0.87$ ), but its performance was generally  
 373 poorer for other parameters. DT, SVM, and RF methods generally showed lower  
 374 performance across all sensitive model parameters. These differences in performance  
 375 highlight the potential benefits of multi-machine learning ensemble methods for  
 376 improving flood prediction in ungauged mountainous catchments.



377  
 378 **Fig.7.** Performance of parameter regionalization methods assessed using Taylor diagrams. The  
 379 diagrams show the accuracy of sensitive model parameter estimates, with the coefficient  
 380 of determination ( $R^2$ ) indicated by the radial axis, standard deviation (STD) by the  
 381 horizontal and vertical axes, root mean square error (RMSE) by the grey-blue dotted lines,  
 382 and the standard deviation of observations by the black dotted line."

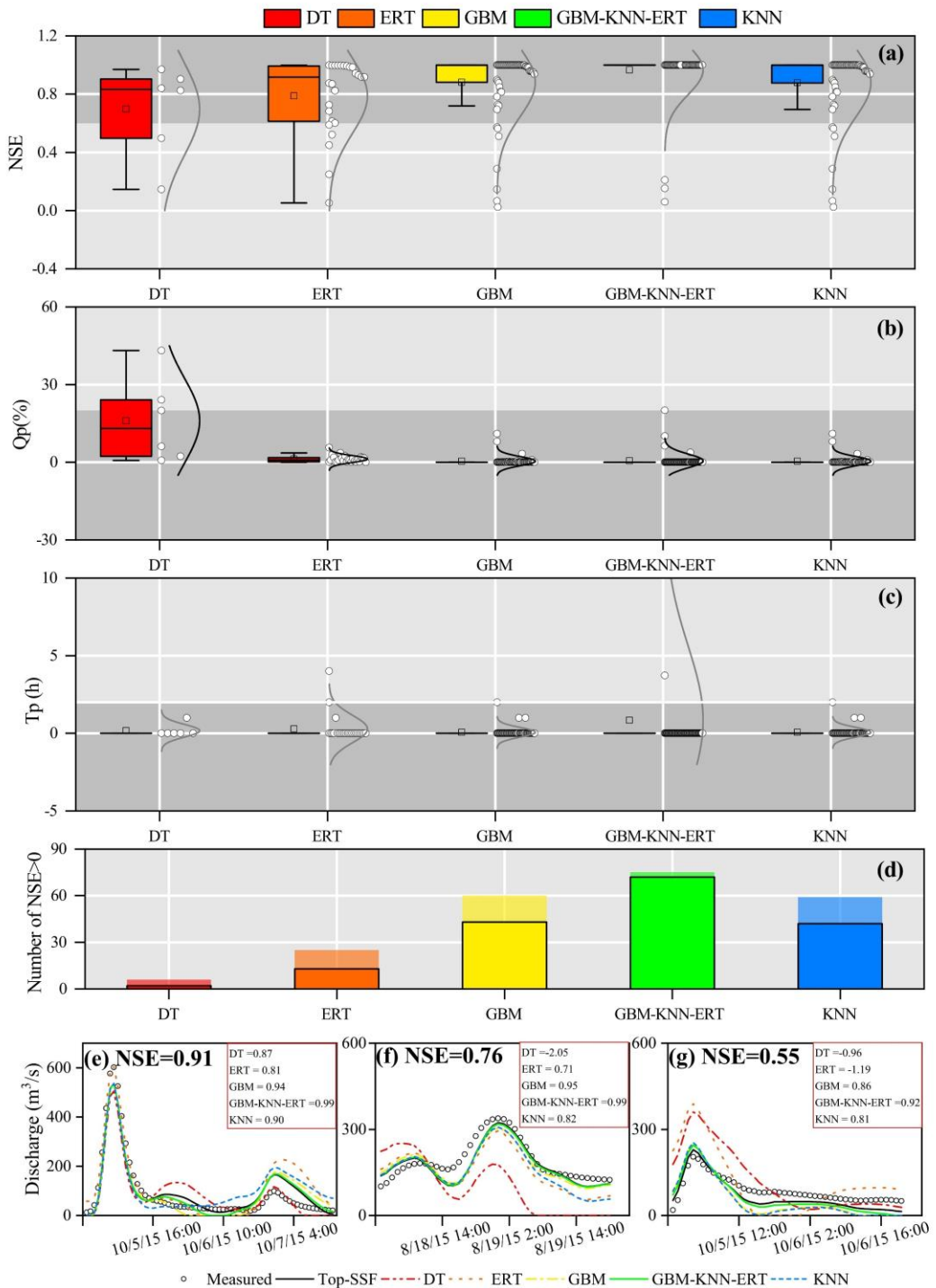
383    **4.2.2. Comparison of flood forecasting results**

384    The flood prediction performance of the Top-SSF model, integrated with different  
385    parameter regionalization methods, was compared across 80 mountainous catchments  
386    in southwestern China. The methods included single machine learning methods and a  
387    multi-machine learning ensemble method (GBM-KNN-ERT), where GBM estimated  
388     $Szm$ ,  $td$ , and  $C$ ; KNN estimated  $lnTe$ ,  $qsf0$ , and  $t$ ; and ERT estimated  $Sfmax$ . The  
389    performance of these parameter regionalization methods was then evaluated against the  
390    performance of the Top-SSF model using calibrated parameters. Among the single  
391    machine learning methods, GBM performed best, with 60 catchments achieving a  
392    positive NSE (NSE > 0, Fig. 8d). Critically, for high-accuracy predictions (NSE > 0.9),  
393    GBM succeeded in 43 catchments (54%), also showing strong performance with  $Qp$   
394    less than 5% and  $Tp$  less than 1 hour in most cases (Fig. 8a-c). The GBM-KNN-ERT  
395    ensemble method yielded even better results. It increased the number of catchments  
396    with positive NSE to 75 (Fig. 8d). More impressively, the ensemble method achieved  
397    exceptional performance (NSE > 0.9) in 72 catchments (90%). This represents a 67.44%  
398    increase in the number of high-accuracy predictions compared to the best single method  
399    (GBM). Furthermore, the ensemble method  $Qp$  values were more concentrated around  
400    zero, and 90% of catchments maintained near-zero  $Tp$  values. These results  
401    demonstrate the superior potential of multi-machine learning ensembles for improving  
402    flood prediction in ungauged catchments.

403    To further illustrate these performance differences visually, Fig. 8 (e, f, and g)  
404    presents hydrographs from three randomly selected flood events. These events

405 represent cases where the calibrated Top-SSF model itself achieved high (NSE=0.91),  
406 medium (NSE=0.76), and low (NSE=0.55) performance, respectively. A key insight  
407 from these plots is that the Top-SSF simulation (solid black line) is the performance  
408 benchmark for the regionalization methods. Although the models aim to approximate  
409 measured floods, their performance is ultimately limited by the accuracy of the Top-  
410 SSF model structure and its optimized parameters.

411 The hydrographs show how the GBM-KNN-ERT ensemble achieves superior  
412 performance by leveraging the complementary strengths of its component methods. For  
413 instance, in the high-performance case (Fig. 8e), the GBM and KNN methods capture  
414 the overall shape well, but the ERT simulation provides a more precise estimation of  
415 the primary flood peak. The final ensemble successfully integrates this peak accuracy,  
416 resulting in the highest overall performance. Similarly, Fig. 8f shows that the ensemble  
417 moderates the slow initial rise characteristic of the KNN method, leading to a more  
418 realistic rising limb. The ensemble method ability to balance competing errors is most  
419 evident in the low-performance case (Fig. 8g). During the recession phase, the ensemble  
420 method averages the high bias of the ERT method with the low bias of the GBM and  
421 KNN methods, producing a hydrograph that more closely resembles the benchmark  
422 simulation than any single method could. This synergy demonstrates that the ensemble  
423 method superior performance is a direct result of its ability to integrate the specific,  
424 complementary strengths of each single method across different parts of the  
425 hydrological process.



426

427

428

429

430

431

432

433

434

435

**Fig.8.** Evaluation of flood prediction performance for different parameter regionalization methods. (a-c) show the distributions of Nash-Sutcliffe Efficiency (NSE), relative peak flow error (Qp), and peak time error (Tp) across all 80 catchments, with shaded regions indicating where flood prediction standards were met ( $\text{NSE} > 0.75$ ,  $\text{Qp} < 20\%$ , and  $\text{Tp} < 2$  hours). (d) shows the number of catchments with  $\text{NSE} > 0$  and the black border indicates the number of catchments with  $\text{NSE} > 0.9$ . (e-g) present example hydrographs comparing the simulated flood from each regionalization method against measured flood flow and the calibrated Top-SSF model benchmark for catchments where the benchmark model performance was (e) high ( $\text{NSE}=0.91$ ), (f) medium ( $\text{NSE}=0.76$ ), and (g) low ( $\text{NSE}=0.55$ ).

436 **5. Discussion**

437 **5.1. Reliability of multi-machine learning ensemble in parameter regionalization**

438 In this study, the GBM-KNN-ERT method demonstrated superior regionalization  
439 performance, highlighting the potential of ensemble methods for improving  
440 hydrological predictions in ungauged mountainous catchments. The success of the  
441 ensemble is rooted in the distinct learning mechanisms and behaviors of its individual  
442 components, which were revealed during hyperparameter optimization.

443 The GBM method exhibited distinct parameter-specific sensitivities to  
444 hyperparameters (Fig. 9a-c). For parameter  $C$ , the negative correlation between  $R^2$  and  
445 n\_estimators ( $>300$  trees) indicates overfitting risks when modeling complex rainfall-  
446 runoff interactions in heterogeneous mountainous terrain (Fig. 9a). This aligns with  
447 previous findings emphasizing the need for complexity control in hydrological  
448 generalization (Schoups et al., 2008). Conversely, the improved  $R^2$  for parameter  $td$   
449 with increased n\_estimators highlights the capacity of ensemble learning to capture  
450 complex, nonlinear relationships between catchment descriptors and hydrological  
451 parameters (Hastie et al., 2009). The contrasting optimal max\_depth of 10 layers for  
452 parameter  $C$ , compared to shallower optimal depths (4 layers) for  $Szm$  and  $td$ , suggests  
453 that parameters governing more complex hydrological processes in mountainous  
454 catchments may require deeper decision trees to effectively capture the interactions  
455 between climate, topography, and soil properties (Wainwright et al., 2013).

456 KNN performance exhibited pronounced sensitivity to neighbourhood size  
457 (n\_neighbors) and distance metric (p), highlighting the spatial heterogeneity of

458 catchment descriptors. For parameters  $lnTe$  and  $qsf0$ , optimal performance was  
459 observed at  $n\_neighbors = 30$  (Fig. 9d), aligns with the hypothesis that meaningful  
460 hydrological similarities can emerge even in topographically complex mountainous  
461 regions when considered at broader spatial scales (Li et al., 2022). Conversely,  
462 parameter  $t$  achieved peak accuracy at  $n\_neighbors=5$ , suggesting that localized, short-  
463 term weather events and fine-scale topographic similarities in adjacent mountainous  
464 areas can significantly influence local runoff processes (Garambois et al., 2015). The  
465 Manhattan distance metric ( $p=1$ ) outperformed Euclidean distance across all  
466 parameters (Fig. 9e). This superiority stems from its ability to mitigate the curse of  
467 dimensionality (Bellman, 1961) in high-dimensional datasets, a common characteristic  
468 of mountainous catchments. In such datasets, sparse data distributions and the presence  
469 of mixed variable types (e.g., topographic indices, land cover) can significantly degrade  
470 the discriminative power of Euclidean distance (Rockström et al., 2023). The  
471 robustness of the Manhattan distance arises from its axis-aligned sensitivity, which  
472 provides a more effective means of handling feature scaling and integrating catchment  
473 descriptors compared to the radial symmetry of Euclidean distance.

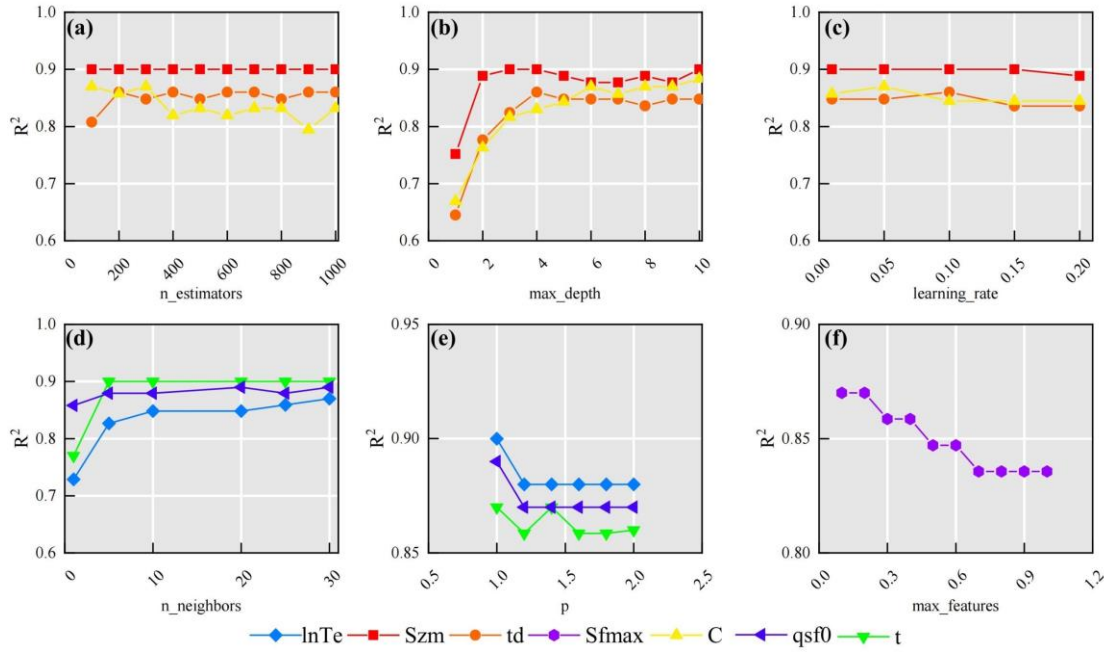
474 ERT performance was maximized at  $max\_features = 0.1$  (Fig. 9f). By restricting  
475 the random sampling of features during node splits (using only 10% of the features),  
476 both the diversity of the trees was enhanced and the effects of multicollinearity between  
477 topographic and soil attributes were reduced. This finding aligns with the theory  
478 proposed by Geurts et al. (2006), which suggests that random feature selection can  
479 significantly improve model generalization, a particularly important consideration in

480 ungauged mountainous catchments characterized by high levels of inter-correlation  
481 among predictor variables.

482 These distinct sensitivities and learning mechanisms form the scientific basis for  
483 the superiority of the GBM-KNN-ERT method. As shown in Section 4.2, no single  
484 machine learning method is universally optimal for all hydrological model parameters.

485 Instead, the ensemble method effectively allocates each parameter to the model best  
486 suited for its regionalization. Specifically, GBM, with its capacity for modeling  
487 complex interactions, proved optimal for integrated parameters like  $Szm$  and  $td$ . In  
488 contrast, the instance-based KNN was superior for parameters like  $lnTe$ , which are  
489 governed by physical similarity and spatial coherence. Finally, the highly randomized  
490 nature of ERT provided the necessary robustness to model the noisy relationship  
491 associated with the  $Sfmax$ . This synergistic combination, where each model  
492 contributes its unique strength, results in a final regionalization method that is more  
493 accurate and physically plausible than any individual method operating in isolation.

494



495  
496 **Fig.9.** Sensitivity of parameter estimation performance to key hyperparameters in (a-c) GBM,  
497 (d-e) KNN method, and (f) ERT. (a) n\_estimators (number of decision trees in GBM), (b)  
498 max\_depth (maximum depth of decision trees in GBM), (c) learning rate (GBM), (d)  
499 n\_neighbors (number of neighbors in KNN), (e) p-value of Minkowski distance (KNN;  
500 p=1: Manhattan distance, p=2: Euclidean distance), and (f) max\_features (ERT).

501

502 **5.2. Combining multiple machine learning methods for parameter regionalization**

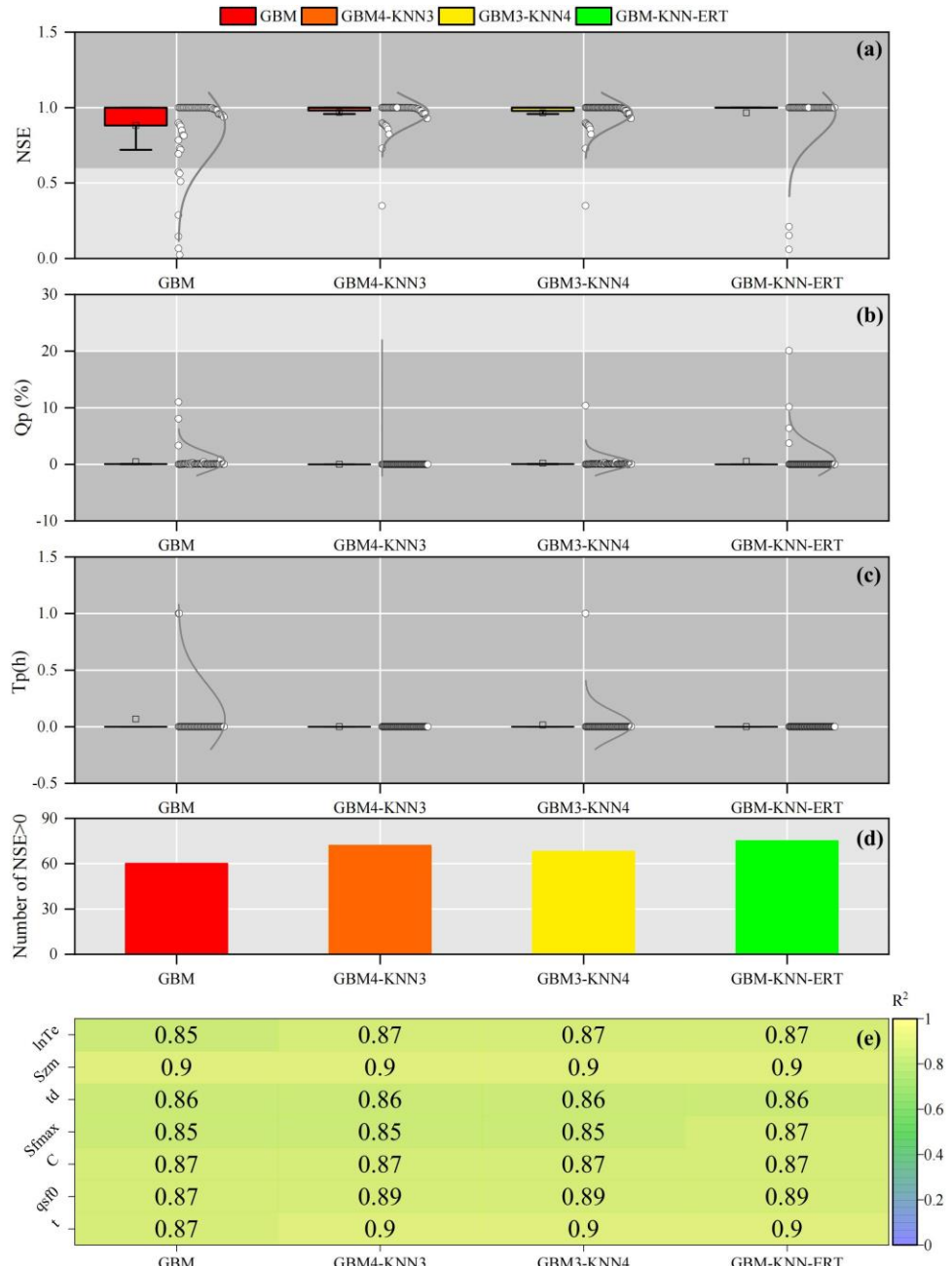
503 Machine learning methods exhibit distinct strengths in hydrological parameter  
504 estimation due to fundamental differences in data processing mechanisms, pattern  
505 recognition strategies, and prediction generation (Bishop et al., 2006). This suggests  
506 that multi-machine learning ensemble methods have the potential to synergistically  
507 integrate advantages while effectively compensating for individual limitations, leading  
508 to more robust and accurate parameter estimates. As demonstrated in Fig. 10, the GBM-  
509 KNN-ERT method achieved notable improvements over any single machine learning  
510 method, particularly for sensitive parameters *lnTe*, *Sfmax*, *qsf0* and *t*, with  $R^2$   
511 increases ranging from 0.02 to 0.03 compared to the best-performing GBM method  
512 (Fig.10e).

513 Interestingly, a comparison of GBM4-KNN3 (where  $Sfmax$  is estimated by GBM)  
514 and GBM3-KNN4 (where  $Sfmax$  is estimated by KNN) revealed critical insights into  
515 model parameter compatibility. Despite both achieving an identical  $R^2$  of 0.85 for the  
516 estimation of  $Sfmax$ , GBM4-KNN3 exhibited superior flood prediction performance,  
517 with 72 catchments achieving  $NSE > 0$  compared to only 68 catchments for GBM3-  
518 KNN4. This suggests that GBM possesses an enhanced capability to resolve the  
519 complex coupling between soil moisture dynamics and topography, leading to more  
520 physically plausible representation of subsurface storm flow processes (Gupta et al.,  
521 2023). The wider distribution of flood prediction performance observed for GBM3-  
522 KNN4 (Fig. 10 a–c) further suggests that uncertainties introduced by KNN in the  
523 estimation of  $Sfmax$  may propagate nonlinearly during flood simulations, potentially  
524 amplifying errors. This observation aligns with theoretical expectations that distance-  
525 based methods may tend to oversmooth critical thresholds or sharp transitions in  
526 heterogeneous environments, leading to a less accurate representation of hydrological  
527 responses (Bellman, 1961).

528 Furthermore, an important consideration in adopting ensemble methods is the  
529 trade-off between predictive accuracy and computational efficiency. To evaluate this  
530 trade-off, the model training times for various parameter regionalization methods were  
531 compared, and the results are summarized in Table 4. The analysis shows that the  
532 proposed GBM-KNN-ERT ensemble, while providing the highest predictive accuracy,  
533 required a total training time of 102.8 s. This is moderately higher than the best-  
534 performing single model, GBM (57.6 s), and other simpler ensemble methods like

535 GBM4-KNN3 (36.1 s). The increased computational time for the GBM-KNN-ERT  
536 method is primarily attributed to the inclusion of the ERT method for estimating the  
537  $S_{fmax}$ , which is inherently more computationally intensive than GBM or KNN.

538 However, it is crucial to contextualize this computational cost for operational use.  
539 The process of training a regionalization method is an offline task, performed once to  
540 establish the stable relationships between catchment descriptors and model parameters.  
541 This one-time investment is not a constraint on real-time flood forecasting, as once the  
542 method is trained, parameter estimation for a new ungauged catchment is nearly  
543 instantaneous. For the reported computational times, all model training and simulations  
544 were performed on a workstation equipped with an Intel(R) Core (TM) i9-10900K CPU  
545 @ 3.70GHz, 32.0 GB of RAM, and an NVIDIA Quadro P1000 (4 GB) GPU, running  
546 on a 64-bit Windows operating system with Python 3.9. Given this context, the modest  
547 increase in one-time training cost is a justifiable investment for the significant  
548 improvements achieved in flood prediction accuracy, model robustness, and stability.  
549 Therefore, for applications in water resource management and flood risk assessment  
550 where high accuracy is paramount, the GBM-KNN-ERT method strikes an optimal and  
551 practical balance between computational efficiency and predictive performance.



552

553 **Fig.10.** Assessment of combined machine learning methods for improved parameter  
 554 regionalization in ungauged mountainous catchments. Performance is evaluated against  
 555 the GBM method, showing (a) NSE, (b) Qp, (c) Tp, (d) Number of catchments with NSE >  
 556 0, and (e) the difference in R<sup>2</sup>.

557

**Table 4.** Running time (s) for different parameter regionalization methods

	GBM	GBM4-KNN3	GBM3-KNN4	GBM-KNN-ERT	KNN	ERT
lnTe	11.3	3.4	3.4	3.7	3.6	74.4
Szm	7.8	7.5	7.7	7.8	0.6	76.7
td	8.2	8.1	8.0	8.5	0.6	74.7
Sfmax	7.7	8.2	0.6	73.6	0.5	74.9
C	7.8	7.7	7.7	8.0	0.6	74.9
qsf0	7.4	0.6	0.6	0.6	0.6	76.3
t	7.4	0.6	0.6	0.6	0.5	75.3
Sum	57.6	36.1	28.6	102.8	7.0	527.2

558 **5.3. The influence of donor catchment quantity on machine-learning parameter**  
559 **regionalization**

560 The number of donor catchments used in machine learning-based parameter  
561 regionalization methods is a critical factor influencing the accuracy and robustness of  
562 hydrological predictions in ungauged catchments (Gauch et al., 2021; Song et al., 2022;  
563 Zhang et al., 2022). This study investigated the influence of donor catchment quantity  
564 (ranging from 20 to 80) on the flood prediction performance of the two best-performing  
565 parameter regionalization methods (GBM4-KNN3 and GBM-KNN-ERT) across the 80  
566 mountainous catchments (Fig.11). It is important to clarify that the following analysis  
567 is not a method for selecting donor catchments based on physical similarity—a task  
568 handled by the machine learning methods itself when it learns the relationships between  
569 catchment descriptors and model parameters. Instead, this experiment serves as a  
570 sensitivity analysis to understand how the regionalization performance is affected by  
571 the overall quantity and quality of the available training data.

572 To systematically investigate the performance influence of donor catchment  
573 quantity on parameter regionalization, two distinct sampling strategies were employed  
574 across the 80 mountainous catchments. In Mode 1 (selection of donor catchments based  
575 on decreasing NSE), which was designed to test the impact of data quality, a non-  
576 monotonic relationship was observed. For both methods, regionalization performance  
577 peaked with 20-40 donor catchments and then declined, particularly for the GBM4-  
578 KNN3 method (Fig. 11a-c). This performance degradation is not due to increasing  
579 catchment dissimilarity, but rather to the introduction of lower-quality training data. As  
580 the donor pool expands beyond the best-performing catchments, it begins to include

581 catchments where the Top-SSF model calibration itself was less successful (i.e., lower  
582 NSE values). These lower-performance samples may introduce noise and less reliable  
583 parameter-descriptor relationships, which can mislead the training process (Gauch et  
584 al., 2021; Zhang et al., 2022). Notably, the GBM-KNN-ERT method demonstrated  
585 greater resilience to this degradation. Its performance, while also peaking early, did not  
586 degrade as sharply and instead tended to stabilize after the inclusion of approximately  
587 70 catchments. This suggests that the more complex ensemble structure has a superior  
588 ability to suppress noise and generalize from a dataset containing a mix of high- and  
589 low-quality examples, highlighting its enhanced robustness. In contrast, Mode 2  
590 (random selection of donor catchments) demonstrated a consistent improvement in  
591 regionalization performance for both NSE and Tp as the number of donor catchments  
592 increased (Fig. 11d-f). However, while the average performance improves with data  
593 quantity, it is important to acknowledge that this trend relies on the random samples  
594 being generally representative; a poorly chosen random set could still reduce  
595 generalizability. Notably, under both modes, the GBM-KNN-ERT method consistently  
596 exhibited significantly greater performance stability compared to the alternative  
597 ensemble, GBM4-KNN3. This enhanced robustness likely arises from its more  
598 effective suppression of data heterogeneity and noise interference, indicating that more  
599 complex ensemble methods possess a greater capacity to balance the benefits of  
600 increased data quantity with the potential drawbacks of reduced data quality.

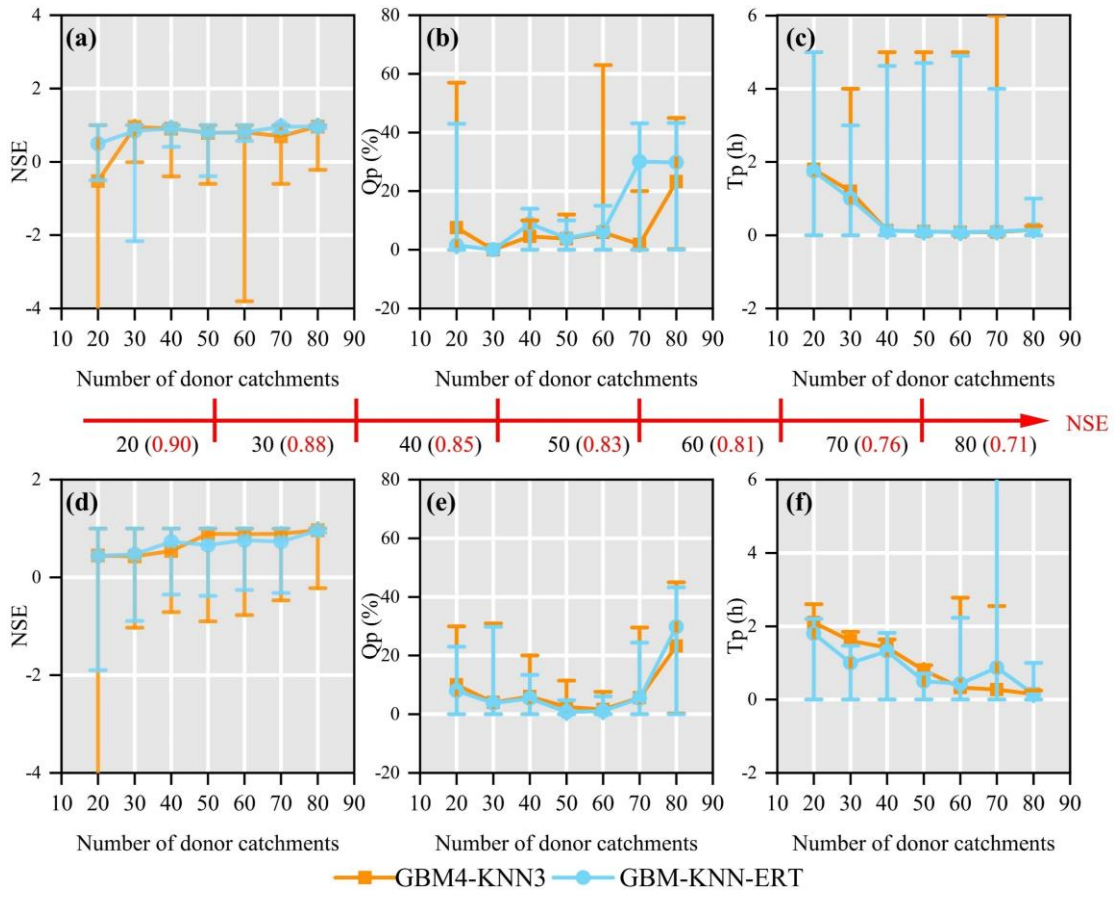


**Fig. 11.** Performance comparison of two donor catchment selection methods for parameter regionalization as a function of donor catchment quantity. Mode1 (a-c) selects donor catchments in order of decreasing NSE, while Mode 2 (d-f) selects them randomly. Flood prediction accuracy is assessed using NSE, Qp, and Tp. Error bars represent the full range (minimum to maximum) of the performance metrics.

#### 5.4. The impact of climate change on parameter regionalization methods

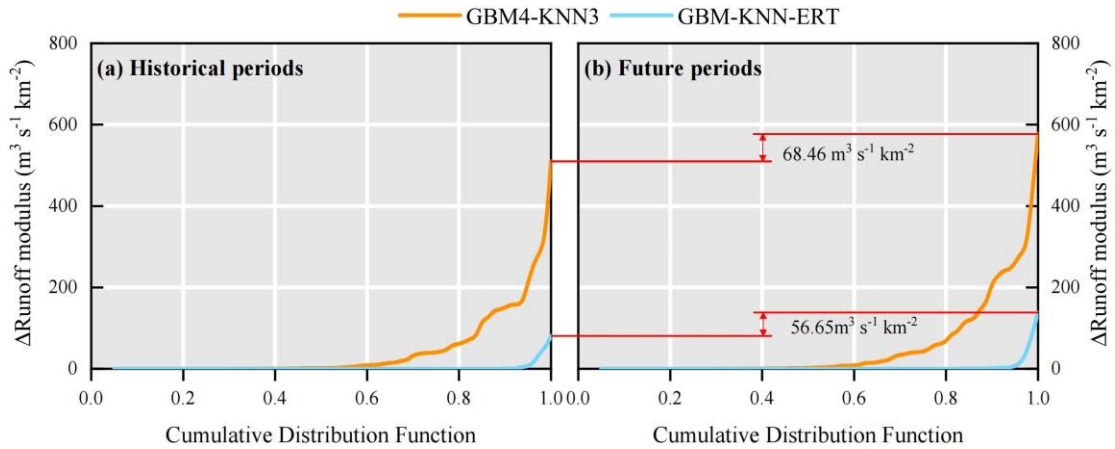
The hydrological cycle within catchments is fundamentally governed by complex interactions between climate and environmental factors. The Intergovernmental Panel on Climate Change (IPCC) has consistently documented a continuous and accelerating transition in global climatic patterns, characterized by increased variability and extreme events (Pachauri et al., 2014). Consequently, future flood predictions derived from parameter regionalization methods are expected to exhibit increased uncertainty and variability, highlighting the substantial influence of climate change on the reliability and precision of flood predictions in ungauged mountainous catchments (Yang et al.,

616 2019). Therefore, a sensitivity analysis was designed to evaluate the robustness of the  
617 trained regionalization models when confronted with climatic conditions outside their  
618 original training range.

619 To quantitatively assess the impact of climate change, an experiment was devised  
620 where this impact was primarily reflected through changes in two key catchment  
621 descriptors: Tem and Pre. For the historical period, these descriptors represent the multi-  
622 year averages over 1901–2021, while for the future period, they represent the projected  
623 multi-year averages over 2022–2100 under the SSP5-8.5 scenario. The regionalization  
624 methods (GBM4-KNN3 and GBM-KNN-ERT), which were trained exclusively using  
625 historical data, were then applied under these future conditions. Crucially, the method  
626 structures and hyperparameters remained fixed, and no retraining was performed; only  
627 the historical Tem and Pre values were replaced with their future projections. This  
628 approach allows the response of the established historical relationships to new, out-of-  
629 sample climatic inputs to be tested. The simulated peak discharges for this analysis were  
630 derived from the same three flood events used in the calibration and validation of the  
631 Top-SSF model. This experimental design is critical as it isolates the impact of the  
632 changed model parameters from the compounding effect of a different future rainfall  
633 event. Consequently, any observed change in the simulated flood peak is attributable  
634 solely to the sensitivity of the regionalization method to the shift in climatic descriptors.  
635 Cumulative distribution functions (CDFs) were then employed to illustrate the  
636 discrepancies between the parameter regionalization simulations and the reference  
637 simulations (derived from calibrated model parameters) across the historical and

638 projected future periods for the 80 catchments (Fig.12).  
639 A comparative analysis of Fig. 12a and 12b reveals a clear amplification of the  
640 absolute differences in predicted flood peaks (quantified as the error in runoff modulus)  
641 between the two parameter regionalization methods and the reference Top-SSF model  
642 simulations during the transition from the historical period to the projected future period.  
643 Specifically, the maximum error in runoff modulus for the GBM4-KNN3 method  
644 increased by  $68.46 \text{ m}^3 \text{ s}^{-1} \text{ km}^{-2}$  from the historical period to the future period, while the  
645 increase for the GBM-KNN-ERT method was a smaller  $56.65 \text{ m}^3 \text{ s}^{-1} \text{ km}^{-2}$ . These results  
646 underscore that parameter regionalization methods are inherently sensitive to changing  
647 climatic forcing. However, they also provide compelling evidence that the GBM-KNN-  
648 ERT method exhibits superior stability and resilience under climate change,  
649 demonstrating its potential for more reliable long-term flood risk assessment in  
650 ungauged mountainous regions.

651 Exploring the effects of climate change on parameter regionalization methods  
652 provides valuable insights for advancing flood prediction research in prediction in  
653 ungauged basins. The enhanced stability demonstrated by the GBM-KNN-ERT  
654 ensemble offers a promising direction for developing robust regionalization methods  
655 capable of navigating the challenges of a non-stationary climate.



656  
657 **Fig.12.** Comparison of flood peak runoff modulus between parameter regionalization and  
658 calibrated Top-SSF model results, showing cumulative distribution functions (CDFs) of  
659 absolute differences for 80 catchments during (a) historical and (b) future periods.

### 660 5.5. Uncertainty and limitation

661 The uncertainty in this study arises from several sources, including the  
662 hydrological model, the regionalization methods, and the data itself. A critical  
663 evaluation of these sources helps to contextualize our findings and assess the  
664 generalizability of the ensemble method. Uncertainty from the hydrological model is  
665 inherent in its structure and the calibrated parameters. Although the Top-SSF model  
666 performed well, its parameters are effective values subject to equifinality. This  
667 uncertainty in the true parameter values can be viewed as a form of calibration bias,  
668 which serves as the target data for our regionalization. To mitigate this, we employed  
669 the robust SCE-UA optimization algorithm and focused only on sensitive parameters.  
670 Uncertainty is also introduced by the regionalization methods themselves, as the  
671 training data derived from donor catchments are susceptible to errors that can impact  
672 model performance (Mosavi et al., 2018; Xu et al., 2021).

673 A specific methodological choice was the exclusion of deep learning architectures,  
674 such as Multilayer Perceptrons or Long Short-Term Memory (LSTM) networks. This

675 decision was guided by several factors. First, parameter regionalization is a static  
676 regression problem, mapping time-invariant catchment descriptors to model parameters,  
677 which does not align with the sequential data structure for which LSTM is designed.  
678 Second, deep networks typically require large datasets to avoid overfitting; with a  
679 dataset of 80 catchments, traditional machine learning methods like GBM and ERT are  
680 often more robust and less prone to memorizing training data. Third, a key advantage  
681 of parameter regionalization is its potential for physical interpretability. Unlike DL  
682 models, whose internal decision-making processes are often obscured within abstract  
683 weight matrices, the ensemble methods employed here offer more accessible  
684 transparency. The tree-based models (GBM and ERT) allow for the direct assessment  
685 of feature importance, enabling the verification of physical consistency. Furthermore,  
686 the KNN component provides instance-based interpretability by explicitly identifying  
687 the specific donor catchments used for transfer. This preserves the traceable logic of  
688 hydrological similarity, clearly indicating the geographical or physical source of the  
689 transferred parameters, which may be crucial for building the trust of the method in the  
690 water management of mountainous catchments.

691 Furthermore, the primary contribution of this study is not the identification of a  
692 single superior algorithm, but the demonstration of a data-driven framework for  
693 constructing a locally optimal ensemble. The complementarity of the chosen models  
694 was not assumed but empirically validated through a competitive evaluation process.  
695 Each of the seven machine learning methods was independently trained and assessed  
696 for its ability to estimate each sensitive parameter. The final GBM-KNN-ERT ensemble

697 was constructed by selecting only the empirically best-performing model for each  
698 parameter based on objective metrics ( $R^2$ , RMSE, STD). The very fact that different  
699 methods were selected for different hydrological parameters provides direct empirical  
700 evidence of their complementary strengths, thus validating the ensemble method.

701 Furthermore, the specific GBM-KNN-ERT ensemble identified is necessarily  
702 data-dependent, raising questions about its transferability. However, this study primary  
703 contribution is not the specific model combination itself, but rather the demonstration  
704 of a data-driven method for constructing a locally optimal ensemble. This method is  
705 designed to be generalizable; applying the same competitive evaluation process to a  
706 new region would identify the best ensemble for that specific dataset. The key to  
707 overcoming these limitations and ensuring robust generalization lies in genuine model  
708 complementarity. The ensemble method's success is not an artifact of overfitting to  
709 calibration bias or data quirks. Instead, it stems from a synergistic integration, where  
710 different models are empirically shown to be better suited for regionalizing parameters  
711 governed by distinct physical processes. The ensemble method's superior stability in  
712 the out-of-sample climate change stress test further supports this conclusion, indicating  
713 that it has captured robust underlying relationships, not just noise.

714 To manage methodological uncertainty, K-fold cross-validation was employed to  
715 ensure robust performance evaluation, and RandomizedSearchCV was used for  
716 hyperparameter tuning to minimize overfitting (Bergstra and Bengio, 2012). A key  
717 methodological decision was to evaluate the regionalization methods against the  
718 outputs of the calibrated Top-SSF model, rather than directly against observed flood

719 events. This approach was chosen for two primary reasons. First, it isolates the  
720 performance of the parameter regionalization itself. The calibrated simulation  
721 represents the theoretical upper bound of performance for the given hydrological model  
722 structure; consequently, any deviation from this benchmark can be directly attributed  
723 to imperfections in the regionalization method, rather than being confounded by the  
724 inherent structural limitations of the Top-SSF model. Second, this strategy ensures that  
725 the machine learning models learn the underlying physical relationships intended by  
726 the hydrological model, not simply mimic data noise or measurement errors present in  
727 the observations. If trained against raw observations, the machine learning methods  
728 might derive spurious parameter sets that compensate for both the hydrological model's  
729 structural flaws and observational errors. Such parameters could appear effective but  
730 would lack physical meaning and generalizability. These measures, combined with the  
731 evidence for model complementarity, provide a strong basis for the scientific validity  
732 and potential for generalization of our proposed ensemble method.

733 **6. Conclusions**

734 This study introduces a novel multi-machine learning ensemble method (GBM-  
735 KNN-ERT) to enhance model parameter transferability and improve flood prediction  
736 in ungauged mountainous catchments. The proposed GBM-KNN-ERT method  
737 demonstrated a substantial advancement in both flood prediction accuracy and model  
738 robustness, achieving exceptional performance with 90% of ungauged catchments  
739 exhibiting a NSE exceeding 0.9, a significant 67.44% improvement compared to the  
740 best single machine learning method evaluated in this study. Importantly, the GBM-

741 KNN-ERT method exhibited remarkable stability under simulated climate change,  
742 thereby highlighting its potential for reliable application in non-stationary hydrological  
743 environments. Furthermore, the method demonstrated notable adaptability to varying  
744 donor-catchment configurations, where an optimal balance between predictive  
745 accuracy and computational efficiency with a relatively limited set of 20–40 high-  
746 quality donor catchments ( $\text{NSE} > 0.85$ ). By integrating the diverse strengths of multiple  
747 machine learning with hydrological model, the proposed methodology significantly  
748 advances the field of flood prediction in ungauged catchments, offering a reliable tool  
749 for water resource management and flood disaster mitigation.

## 750 **Acknowledgements**

751 This research was supported by the Joint Funds of the National Natural Science  
752 Foundation of China (**U2240226**), the National Natural Science Foundation of China  
753 (**42271038**) and the National Key Research and Development Program of China  
754 (**2022FY100205**).

## 755 **Competing interests**

756 The authors declare that they have no known competing financial interests or  
757 personal relationships that could have appeared to influence the work reported in this  
758 paper.

## 759 **Author contributions**

760 In this study, K L, G W, and J G were responsible for the conceptualization of the  
761 research. Data curation was carried out by K L, L G, and X S, while formal analysis  
762 was performed by K L, J G, and J M. The methodology was developed by K L, L G, P

763 H, and J L. Project administration was overseen by G W and J G. K L took the lead in  
764 writing the original draft, and the writing, review, and editing process involved  
765 contributions from K L, G W, J L, P H, J M, X Z, and J G.

## 766 **Code and data availability**

767 The code used in this study is available upon request from the authors. The  
768 meteorological, soil characteristics, and topography datasets are publicly accessible  
769 online, as detailed in Table 1. The hourly flood data for the 80 catchments were sourced  
770 from China's Hydrological Yearbook. These data are not publicly available due to  
771 governmental restrictions but can be accessed by contacting the corresponding author  
772 for further information.

## 773 **References**

774 Arsenault, R., Breton-Dufour, M., Poulin, A., Dallaire, G. Romero-Lopez, R. (2019).  
775 Streamflow prediction in ungauged basins: analysis of regionalization methods  
776 in a hydrologically heterogeneous region of Mexico. *Hydrological Sciences  
777 Journal*, 64(11): 1297-1311. <https://doi.org/10.1080/02626667.2019.1639716>

778 Arsenault, R., Martel, J., Mai, J. (2022). Continuous streamflow prediction in ungauged  
779 basins: Long Short-Term Memory Neural Networks clearly outperform  
780 hydrological models. *Hydrol. Earth Syst. Sci.* 1-29.  
<https://doi.org/10.5194/hess-27-139-2023>

782 Bellman, R.E. (1961). On the reduction of dimensionality for classes of dynamic  
783 programming processes. RAND Corp., Santa Monica, Calif., Paper P-2243.

784 Bergstra, J. Bengio, Y. (2012). Random search for hyper-parameter optimization.  
785 *Journal of machine learning research*, 13(2).

786 Beven, K.J., Kirkby, M.J., Freer, J.E., Lamb, R. (2021). A history of TOPMODEL.  
787 *Hydrology and Earth System Sciences*, 25(2): 527-549.  
<https://doi.org/10.5194/hess-25-527-2021S>

789 Bishop, C.M. Nasrabadi, N.M., (2006). *Pattern recognition and machine learning  
790 (information science and statistics)*. New York: Springer - Verlag.

791 Breiman, L. (2001). Random forests. *Machine learning*, 45: 5-32.

792 Cheng, Q., Gao, L., Zuo, X. Zhong, F. (2019). Statistical analyses of spatial and  
793 temporal variabilities in total, daytime, and nighttime precipitation indices and  
794 of extreme dry/wet association with large-scale circulations of Southwest China,

1961–2016. Atmospheric research, 219: 166-182.  
<https://doi.org/10.1109/ACCESS.2018.2886549>

Choi, J., Kim, U.Kim, S. (2023). Ecohydrologic model with satellite-based data for predicting streamflow in ungauged basins. *Science of The Total Environment*, 903: 166617. <https://doi.org/10.1016/j.scitotenv.2023.166617>

Dai, Y., Shangguan, W., Duan, Q., Liu, B., Fu, S.Niu, G. (2013). Development of a China dataset of soil hydraulic parameters using pedotransfer functions for land surface modeling. *Journal of Hydrometeorology*, 14(3): 869-887. <https://doi.org/10.1175/JHM-D-12-0149.1>

Dakhlaoui, H., Bargaoui, Z.Bárdossy, A. (2012). Toward a more efficient calibration schema for HBV rainfall–runoff model. *Journal of Hydrology*, 444: 161-179. <https://doi.org/10.1016/j.jhydrol.2012.04.015>

Ding, Y.Peng, S. (2020). Spatiotemporal trends and attribution of drought across China from 1901–2100. *Sustainability*, 12(2): 477. <https://doi.org/10.3390/su12020477>

Duan, Q., Sorooshian, S.Gupta, V.K. (1994). Optimal use of the SCE-UA global optimization method for calibrating watershed models. *Journal of Hydrology*, 158(3): 265-284. [https://doi.org/10.1016/0022-1694\(94\)90057-4](https://doi.org/10.1016/0022-1694(94)90057-4)

Friedman, J.H. (2002). Stochastic gradient boosting. *Computational statistics & data analysis*, 38(4): 367-378. [https://doi.org/10.1016/S0167-9473\(01\)00065-2](https://doi.org/10.1016/S0167-9473(01)00065-2)

Gan, B., Liu, X., Yang, X., Wang, X.Zhou, J. (2018). The impact of human activities on the occurrence of mountain flood hazards: lessons from the 17 August 2015 flash flood/debris flow event in Xuyong County, south-western China. *Geomatics, Natural Hazards and Risk*, 9(1): 816-840. <https://doi.org/10.1080/19475705.2018.1480539>

Gao, J., Kirkby, M.Holden, J. (2018). The effect of interactions between rainfall patterns and land-cover change on flood peaks in upland peatlands. *Journal of Hydrology*, 567: 546-559. <https://doi.org/10.1016/j.jhydrol.2018.10.039>

Garambois, P.A., Roux, H., Larnier, K., Labat, D.Dartus, D. (2015). Parameter regionalization for a process-oriented distributed model dedicated to flash floods. *Journal of Hydrology*, 525: 383-399. <https://doi.org/10.1016/j.jhydrol.2015.03.052>

Gauch, M., Mai, J.Lin, J. (2021). The proper care and feeding of CAMELS: How limited training data affects streamflow prediction. *Environmental Modelling & Software*, 135: 104926. <https://doi.org/10.1016/j.envsoft.2020.104926>

Geurts, P., Ernst, D.Wehenkel, L. (2006). Extremely randomized trees. *Machine Learning*, 63(1): 3-42. <https://doi.org/10.1007/s10994-006-6226-1>

Golian, S., Murphy, C.Meresa, H. (2021). Regionalization of hydrological models for flow estimation in ungauged catchments in Ireland. *Journal of Hydrology: Regional Studies*, 36: 100859. <https://doi.org/10.1016/j.ejrh.2021.100859>

Guo, L., Huang, K., Wang, G.Lin, S. (2022). Development and evaluation of temperature-induced variable source area runoff generation model. *Journal of Hydrology*, 610: 127894. <https://doi.org/10.1016/j.jhydrol.2022.127894>

838 Guo, Y., Zhang, Y., Zhang, L.Wang, Z. (2021). Regionalization of hydrological  
839 modeling for predicting streamflow in ungauged catchments: A comprehensive  
840 review. Wiley Interdisciplinary Reviews: Water, 8(1): e1487.  
841 <https://doi.org/10.1002/wat2.1487>

842 Gupta, A.K., Chakroborty, S., Ghosh, S.K.Ganguly, S. (2023). A machine learning  
843 model for multi-class classification of quenched and partitioned steel  
844 microstructure type by the k-nearest neighbor algorithm. Computational  
845 Materials Science, 228: 112321.  
846 <https://doi.org/10.1016/j.commatsci.2023.112321>

847 Hastie, T., Tibshirani, R.Friedman, J., (2009). The elements of statistical learning.  
848 Citeseer.

849 Hersbach, H., Bell, B., Berrisford, P., Biavati, G., Horányi, A., Muñoz Sabater, J.,  
850 Nicolas, J., Peubey, C., Radu, R., Rozum, I., Schepers, D., Simmons, A., Soci,  
851 C., Dee, D.Thépaut, J.-N., (2023). ERA5 hourly data on single levels from 1940  
852 to present, Copernicus Climate Change Service (C3S) Climate Data Store  
853 (CDS)[Dataset]. <https://doi.org/10.24381/cds.adbb2d47> (Accessed on 08-06-  
854 2023)

855 Hua, F., Wang, L., Fisher, B., Zheng, X., Wang, X., Douglas, W.Y., Tang, Y., Zhu,  
856 J.Wilcove, D.S. (2018). Tree plantations displacing native forests: The nature  
857 and drivers of apparent forest recovery on former croplands in Southwestern  
858 China from 2000 to 2015. Biological Conservation, 222: 113-124.  
859 <https://doi.org/10.1016/j.biocon.2018.03.034>

860 Jordan, M.I.Mitchell, T.M. (2015). Machine learning: Trends, perspectives, and  
861 prospects. Science, 349(6245): 255-260. <https://doi.org/10.1126/science.aaa841>

862 Jung, Y. (2018). Multiple predicting K-fold cross-validation for model selection.  
863 Journal of Nonparametric Statistics, 30(1): 197-215.  
864 <https://doi.org/10.1080/10485252.2017.1404598>

865 Kanishka, G.Eldho, T. (2017). Watershed classification using isomap technique and  
866 hydrometeorological attributes. Journal of Hydrologic Engineering, 22(10):  
867 04017040. [https://doi.org/10.1061/\(ASCE\)HE.1943-5584.0001562](https://doi.org/10.1061/(ASCE)HE.1943-5584.0001562)

868 Kratzert, F., Klotz, D., Herrnegger, M., Sampson, A.K., Hochreiter, S.Nearing, G.S.  
869 (2019). Toward improved predictions in ungauged basins: Exploiting the power  
870 of machine learning. Water Resources Research, 55(12): 11344-11354.  
871 <https://doi.org/10.1029/2019WR026065>

872 Lenhart, T., Eckhardt, K., Fohrer, N.Frede, H.G. (2002). Comparison of two different  
873 approaches of sensitivity analysis. Physics and Chemistry of the Earth, Parts  
874 A/B/C, 27(9): 645-654. [https://doi.org/10.1016/S1474-7065\(02\)00049-9](https://doi.org/10.1016/S1474-7065(02)00049-9)

875 Li, K., Wang, G., Gao, J., Guo, L., Li, J.Guan, M. (2024). The rainfall threshold of  
876 forest cover for regulating extreme floods in mountainous catchments. Catena,  
877 236: 107707. <https://doi.org/10.1016/j.catena.2023.107707>

878 Li, X., Khandelwal, A., Jia, X., Cutler, K., Ghosh, R., Renganathan, A., Xu, S., Tayal,  
879 K., Nieber, J.Duffy, C. (2022). Regionalization in a global hydrologic deep  
880 learning model: from physical descriptors to random vectors. Water Resources  
881 Research, 58(8): e2021WR031794. <https://doi.org/10.1029/2021WR031794>

882 Li, Z., Xu, X., Yu, B., Xu, C., Liu, M. Wang, K. (2016). Quantifying the impacts of  
883 climate and human activities on water and sediment discharge in a karst region  
884 of southwest China. *Journal of Hydrology*, 542: 836-849.  
885 <https://doi.org/10.1016/j.jhydrol.2016.09.049>

886 Liu, C., Guo, L., Ye, L., Zhang, S., Zhao, Y. Song, T. (2018). A review of advances in  
887 China's flash flood early-warning system. *Natural hazards*, 92: 619-634.  
888 <https://doi.org/10.1007/s11069-018-3173-7>

889 Luo, P., He, B., Takara, K., Xiong, Y.E., Nover, D., Duan, W. Fukushi, K. (2015).  
890 Historical assessment of Chinese and Japanese flood management policies and  
891 implications for managing future floods. *Environmental Science & Policy*, 48:  
892 265-277. <https://doi.org/10.1016/j.envsci.2014.12.015>

893 McMillan, H.K. (2021). A review of hydrologic signatures and their applications. *Wiley  
894 Interdisciplinary Reviews: Water*, 8(1): e1499.  
895 <https://doi.org/10.1002/wat2.1499>

896 Morel-Seytoux, H.J. Khanji, J. (1974). Derivation of an equation of infiltration. *Water  
897 Resources Research*, 10(4): 795-800.  
898 <https://doi.org/10.1029/WR010i004p00795>

899 Mosavi, A., Ozturk, P. Chau, K.w. (2018). Flood prediction using machine learning  
900 models: Literature review. *Water*, 10(11): 1536.  
901 <https://doi.org/10.3390/w10111536>

902 Nearing, G., Cohen, D., Dube, V., Gauch, M., Gilon, O., Harrigan, S., Hassidim, A.,  
903 Klotz, D., Kratzert, F., Metzger, A., Nevo, S., Pappenberger, F., Prudhomme, C.,  
904 Shalev, G., Shenzis, S., Tekalign, T.Y., Weitzner, D. Matias, Y. (2024). Global  
905 prediction of extreme floods in ungauged watersheds. *Nature*, 627(8004): 559-  
906 563. <https://doi.org/10.1038/s41586-024-07145-1>

907 Pachauri, R.K., Allen, M.R., Barros, V.R., Broome, J., Cramer, W., Christ, R., Church,  
908 J.A., Clarke, L., Dahe, Q. Dasgupta, P., (2014). Climate change 2014: synthesis  
909 report. Contribution of Working Groups I, II and III to the fifth assessment  
910 report of the Intergovernmental Panel on Climate Change.

911 Papageorgaki, I. Nalbantis, I. (2016). Classification of Drainage Basins Based on  
912 Readily Available Information. *Water Resources Management*, 30(15): 5559-  
913 5574. <https://doi.org/10.1007/s11269-016-1410-y>

914 Pugliese, A., Persiano, S., Bagli, S., Mazzoli, P., Parajka, J., Arheimer, B., Capell, R.,  
915 Montanari, A., Blöschl, G. Castellarin, A. (2018). A geostatistical data-  
916 assimilation technique for enhancing macro-scale rainfall-runoff simulations.  
917 *Hydrology and Earth System Sciences*, 22(9): 4633-4648.  
918 <https://doi.org/10.5194/hess-22-4633-2018>

919 Qi, W., Zhang, C., Fu, G. Zhou, H. (2016). Quantifying dynamic sensitivity of  
920 optimization algorithm parameters to improve hydrological model calibration.  
921 *Journal of Hydrology*, 533: 213-223.  
922 <https://doi.org/10.1016/j.jhydrol.2015.11.052>

923 Ragettli, S., Zhou, J., Wang, H., Liu, C. Guo, L. (2017). Modeling flash floods in  
924 ungauged mountain catchments of China: A decision tree learning approach for

925 parameter regionalization. *Journal of Hydrology*, 555: 330-346.  
926 <https://doi.org/10.1016/j.jhydrol.2017.10.031>

927 Rockström, J., Gupta, J., Qin, D., Lade, S.J., Abrams, J.F., Andersen, L.S., Armstrong  
928 McKay, D.I., Bai, X., Bala, G., Bunn, S.E., Ciobanu, D., DeClerck, F., Ebi, K.,  
929 Gifford, L., Gordon, C., Hasan, S., Kanie, N., Lenton, T.M., Loriani, S.,  
930 Liverman, D.M., Mohamed, A., Nakicenovic, N., Obura, D., Ospina, D.,  
931 Prodani, K., Rammelt, C., Sakschewski, B., Scholtens, J., Stewart-Koster, B.,  
932 Tharammal, T., van Vuuren, D., Verburg, P.H., Winkelmann, R., Zimm, C.,  
933 Bennett, E.M., Bringezu, S., Broadgate, W., Green, P.A., Huang, L., Jacobson,  
934 L., Ndehedehe, C., Pedde, S., Rocha, J., Scheffer, M., Schulte-Uebbing, L., de  
935 Vries, W., Xiao, C., Xu, C., Xu, X., Zafra-Calvo, N.Zhang, X. (2023). Safe and  
936 just Earth system boundaries. *Nature*, 619(7968): 102-111.  
937 <https://doi.org/10.1038/s41586-023-06083-8>

938 Sain, S.R. (1996). The Nature of Statistical Learning Theory. *Technometrics*, 38(4):  
939 409-409. <https://doi.org/10.1080/00401706.1996.10484565>

940 Salmeron, R., García, C.García, J. (2018). Variance inflation factor and condition  
941 number in multiple linear regression. *Journal of statistical computation and  
942 simulation*, 88(12): 2365-2384.  
943 <https://doi.org/10.1080/00949655.2018.1463376>

944 Schoups, G., van de Giesen, N.C.Savenije, H.H.G. (2008). Model complexity control  
945 for hydrologic prediction. *Water Resources Research*, 44(12).  
946 <https://doi.org/10.1029/2008WR006836>

947 Shangguan, W., Dai, Y., Liu, B., Zhu, A., Duan, Q., Wu, L., Ji, D., Ye, A., Yuan,  
948 H.Zhang, Q. (2013). A China data set of soil properties for land surface  
949 modeling. *Journal of Advances in Modeling Earth Systems*, 5(2): 212-224.  
950 <https://doi.org/10.1002/jame.20026>

951 Song, Z., Xia, J., Wang, G., She, D., Hu, C.Hong, S. (2022). Regionalization of  
952 hydrological model parameters using gradient boosting machine. *Hydrology  
953 and Earth System Sciences*, 26(2): 505-524. <https://doi.org/10.5194/hess-26-505-2022>

955 Tang, S., Sun, F., Liu, W., Wang, H., Feng, Y.Li, Z. (2023). Optimal Postprocessing  
956 Strategies With LSTM for Global Streamflow Prediction in Ungauged Basins.  
957 *Water Resources Research*, 59(7): e2022WR034352.  
958 <https://doi.org/10.1029/2022WR034352>

959 Wainwright, J.Mulligan, M., (2013). Environmental modelling: finding simplicity in  
960 complexity. John Wiley & Sons.

961 Wani, O., Beckers, J.V.L., Weerts, A.H.Solomatine, D.P. (2017). Residual uncertainty  
962 estimation using instance-based learning with applications to hydrologic  
963 forecasting. *Hydrol. Earth Syst. Sci.*, 21(8): 4021-4036.  
964 <https://doi.org/10.5194/hess-21-4021-2017>

965 Wu, H., Zhang, J., Bao, Z., Wang, G., Wang, W., Yang, Y.Wang, J. (2022). Runoff  
966 modeling in ungauged catchments using machine learning algorithm-based  
967 model parameters regionalization methodology. *Engineering*.  
968 <https://doi.org/10.1016/j.eng.2021.12.014>

969 Xu, Q., Chen, J., Peart, M.R., Ng, C.-N., Hau, B.C.H.Law, W.W.Y. (2018). Exploration  
970 of severities of rainfall and runoff extremes in ungauged catchments: A case  
971 study of Lai Chi Wo in Hong Kong, China. *Science of The Total Environment*,  
972 634: 640-649. <https://doi.org/10.1016/j.scitotenv.2018.04.024>

973 Xu, T.Liang, F. (2021). Machine learning for hydrologic sciences: An introductory  
974 overview. *Wiley Interdisciplinary Reviews: Water*, 8(5).  
975 <https://doi.org/10.1002/wat2.1533>

976 Yang, X., Magnusson, J., Rizzi, J.Xu, C.-Y. (2018). Runoff prediction in ungauged  
977 catchments in Norway: comparison of regionalization approaches. *Hydrology*  
978 *Research*, 49(2): 487-505. <https://doi.org/10.2166/nh.2017.071>

979 Yang, X., Magnusson, J.Xu, C.Y. (2019). Transferability of regionalization methods  
980 under changing climate. *Journal of Hydrology*, 568: 67-81.  
981 <https://doi.org/10.1016/j.jhydrol.2018.10.030>

982 Zhai, X., Guo, L., Liu, R.Zhang, Y. (2018). Rainfall threshold determination for flash  
983 flood warning in mountainous catchments with consideration of antecedent soil  
984 moisture and rainfall pattern. *Natural Hazards*, 94: 605-625.  
985 <https://doi.org/10.1007/s11069-018-3404-y>

986 Zhang, B., Ouyang, C., Cui, P., Xu, Q., Wang, D., Zhang, F., Li, Z., Fan, L., Lovati, M.,  
987 Liu, Y.Zhang, Q. (2024). Deep learning for cross-region streamflow and flood  
988 forecasting at a global scale. *The Innovation*, 5(3).  
989 <https://doi.org/10.1016/j.xinn.2024.100617>

990 Zhang, Y., Chiew, F.H., Li, M.Post, D. (2018). Predicting runoff signatures using  
991 regression and hydrological modeling approaches. *Water Resources Research*,  
992 54(10): 7859-7878. <https://doi.org/10.1029/2018WR023325>

993 Zhang, Y., Chiew, F.H., Liu, C., Tang, Q., Xia, J., Tian, J., Kong, D.Li, C. (2020). Can  
994 remotely sensed actual evapotranspiration facilitate hydrological prediction in  
995 ungauged regions without runoff calibration? *Water Resources Research*, 56(1):  
996 e2019WR026236. <https://doi.org/10.1029/2019WR026236>

997 Zhang, Y., Ragettli, S., Molnar, P., Fink, O.Peleg, N. (2022). Generalization of an  
998 Encoder-Decoder LSTM model for flood prediction in ungauged catchments.  
999 *Journal of Hydrology*, 614: 128577.  
1000 <https://doi.org/10.1016/j.jhydrol.2022.128577>

1001 Zounemat-Kermani, M., Batelaan, O., Fadaee, M.Hinkelmann, R. (2021). Ensemble  
1002 machine learning paradigms in hydrology: A review. *Journal of Hydrology*, 598:  
1003 126266. <https://doi.org/10.1016/j.jhydrol.2021.126266>

1004